Title

From Urban Fires to Industrial Plumes: Toward Routine Quantification of Urban Point Source Emissions of Greenhouse Gases and Aerosols

ISBN

9798189270789

Author

Patel, Milan Yogesh

Publication Date

2026-05-01

Peer reviewed|Thesis/dissertation

From Urban Fires to Industrial Plumes: Toward Routine Quantification of Urban Point Source Emissions of Greenhouse Gases and Aerosols

by

Milan Yogesh Patel

A dissertation submitted in partial satisfaction of the

requirements for the degree of

Doctor of Philosophy

in

Chemistry

in the

Graduate Division

of the

University of California, Berkeley

Committee in charge:

Professor Ronald C. Cohen, Chair
Professor Kristie A. Boering
Professor Allen H. Goldstein

Spring 2026

From Urban Fires to Industrial Plumes: Toward Routine Quantification of Urban Point Source Emissions of Greenhouse Gases and Aerosols

Abstract

From Urban Fires to Industrial Plumes: Toward Routine Quantification of Urban Point Source Emissions of Greenhouse Gases and Aerosols

by

Milan Yogesh Patel

Doctor of Philosophy in Chemistry

University of California, Berkeley

Professor Ronald C. Cohen, Chair

The rise of urban areas as the predominant residence for the world's population has positioned cities as leading contributors to global greenhouse gas and air pollutant emissions. In order to mitigate emissions and their effects efficiently, it is crucial to have a thorough understanding of the urban emission landscape, which remains a challenge given the heterogeneity of emission sources within cities. The atmospheric observation network continues to expand as more and more measurements from satellites, mobile monitoring and aircraft campaigns, and sparse stationary monitoring sites are being made. These observation techniques provide useful information at a wide variety of spatial and temporal scales, but gaps in our understanding of urban air quality still persist. Dense sensor networks fill a niche measurement gap in our current observing system by providing long-term, high frequency measurements of air pollutants at high spatial density across target areas. These measurement networks provide a unique opportunity to study details of the urban emission landscape, including local spatial variability, transient events, and long-term trends of neighborhood-level emission patterns. In this work, we use the Berkeley Environmental Air-quality and CO_2 Network ($BEACO_2N$) to explore the multitude of ways at which dense sensor networks can provide unique insights to both air pollutant and CO_2 emissions within cities.

We start by outlining a calibration methodology for the Plantower PMS5003 sensor to generate robust measurements of ambient $PM_{2.5}$. We adopt a physics-based model to account for changes in particle size due to hygroscopic growth–the uptake of water onto particles based on ambient humidity and the hygroscopicity of the particle. Using $BEACO_2N$ data in the San Francisco Bay Area and in Los Angeles, CA, we find unique seasonal cycles of hygroscopicity that match with particle composition measurements and employ these empirical measures of hygroscopicity to calibrate the Plantower sensor. We then use the $BEACO_2N$ network to quantify emissions of air pollutants and CO_2 from different point sources. We start with a transient pollution event, a small urban fire in Albany, CA, where the spatial

density of sensors is used to constrain the shape of the pollutant plume over time using a 2-D Gaussian model. We calculate the total emissions of $PM_{2.5}$, CO, NO_x, and CO_2. Using this case study, we explore the extent to which dense sensor networks can quantify point source emissions by calculating limits of detection and quantification for the $BEACO_2N$ network. We then use the $BEACO_2N$ network to quantify air pollutant and CO_2 emissions from a continuous point source emitter, namely the Richmond Chevron Refinery in Richmond, CA. Using the Gaussian plume model and several hundred plume observations made over 2 years, we calculate the CO_2 emission rate for the refinery and find it in good agreement with external inventories and measurements. We additionally calculate a CO emission rate, not previously constrained by external observations, and find that inventories likely severely underestimate CO emissions from the refinery. We conclude by describing prospects for detection and characterization of other point emission sources, including preliminary work on maritime shipping emissions.

Overall, the work here shows that low-cost, dense sensor networks provide unique insight into emission sources within urban areas. Given the increasing deployment of similar networks across the globe, the methods explored here show great promise for unlocking insights into pollutant sources, emission magnitudes, and trends in greenhouse gases and air quality in cities worldwide.

To My Family

Contents

List of Figures

List of Tables

Acknowledgments

None of the work presented here would have ever come to fruition without the incredible support of the amazing people in my life, far too many to list here, that have provided me never-ending support, guidance, and motivation over the last 5 years.

First and foremost, I want to thank my advisor, Ron Cohen, for his unwavering support and for all of the wisdom and knowledge he has given me. It was illuminating to see the world through his perspective, and I could not have asked for a better advisor during my time at Berkeley.

Thank you to Professors Kristie Boering and Allen Goldstein, who have kindly and continuously provided feedback throughout my time here, during my qualifying exam, at group meeting presentations, and in writing this dissertation.

Naomi and Pietro, I couldn't have asked for better mentors both inside and outside of the lab as I tried to find my footing as a graduate student. Your spirits and passion made it a treat to show up to lab every day, and your patience showed no bounds even though my questions never ended.

To Sam, my chem-mentee turned coworker and friend, thanks for always being free to chat even in the busiest of times. To Danika, Natalie, and Serena, thanks for being such amazingly fun and welcoming labmates, I know the lab group culture will stay top-ranked in your hands. To Raffy and Toireasa, thank you for always bringing a youthful and vibrant energy to the office, I can't wait to follow along on your journeys.

Thanks to all of the friends I've made at Berkeley along the way. All of the weekend trips, game nights, hiking expeditions, lunch catch-ups, Thanksgiving feasts, and Taco Tuesdays were a much needed reprieve from the day-to-day.

Thank you to my Mom and Dad, who have always supported me every step of the way, even when I decided to move so far from home to embark on this journey. It is only because of their hard work and selflessness that I find myself on this path. Thank you to my brother, Anand, and my sister, Priya, for always being there when I need them. It is in following their example that I strive to become the best version of myself.

Finally and most importantly, to Anna and Yishu, my B70A Office Buddies™, I cannot imagine having gone through this experience without you both. You were always by my side (literally and figuratively) every single day, whether I was at my best or at my worst. Your friendships are truly the greatest gifts to come from this experience. Just as we started, let us finish this journey side-by-side so we can start the next chapter.

Chapter 1

Introduction

1.1 Understanding the Urban Atmosphere

Cities house a growing proportion of the world's population, with 55% of the global population currently living in urban areas and a projected 68% living in urban areas by 2050.[1] Increased activity within these urban centers leads to cities having outsized effects on pollutant emissions into the atmosphere. It is estimated that cities are currently responsible for 70% of CO_2-equivalent greenhouse gas (GHG) emissions, making them prime locations for targeted greenhouse gas mitigation efforts in the fight against climate change.[2] Additionally, cities tend to have substantially worse air quality due to emissions of air pollutants like nitrogen oxides, volatile organic compounds, and particulate matter, which are directly harmful to exposed populations and chemically react in the atmosphere to produce additional harmful pollutants like ozone and secondary aerosol. Air pollution is the second leading cause of premature death across the globe, responsible for roughly 8 million deaths each year.[3] Cities are drivers of air pollution exposure by bringing people and pollution sources in close proximity, though this also situates cities as prime locations for mitigating the health impacts of air pollution.[4] Despite the contrast between the global scale of GHG-induced climate impacts and the relatively local health effects of air pollutants, the goals of mitigating climate change and air pollution are inextricably linked by common emission sources and pathways. Having a thorough understanding of air composition within cities is necessary to understand processes and guide policies targeted at reducing greenhouse gas emissions and improving air quality and public health. However, the confluence of emission sources within cities leads to a complex and heterogeneous landscape which requires detailed analysis to understand sources and subsequent concentration and exposure landscapes with the necessary spatial and temporal resolution.

1.2 The Current State of Atmospheric Observing Systems

A wide variety of in situ and remote sensing observational platforms have been deployed to study atmospheric composition at a variety of spatial and temporal scales and resolutions. Of particular interest to the investigation of urban emissions is the concentration of species near the surface. Here, I highlight some of the many observational techniques advanced over the past several decades for studying tropospheric composition, particularly in and around urban centers.

Satellites have emerged as a key observational tool for targeted measurements of both greenhouse gases (OCO-2, OCO-3, Tanager-1, GHGSat, GOSAT, MethaneSAT, etc.) and air pollutants (OMI, TROPOMI, TEMPO, GEMS, Sentinel-4, etc.).[5–7] Satellites offer the benefit of broad spatial coverage, with global coverage for polar-orbiting satellites and continental coverage for geostationary satellites. These satellites are often operational for many years, allowing long-term analysis of air composition trends. While many of these satellites are relatively new, scientists have made use of imaging satellites (Landsat, Sentinel-2, etc.), which have many years of existing imagery, to extract historical information about extreme events affecting air composition as well.[7] While satellite products offer broad scope information about the atmosphere, they are often limited either in spatial resolution or in measurement frequency at a given location, hindering analysis of small-scale and transient pollution events and trends. Aircraft campaigns use similar remote sensing techniques as well as in situ sampling for targeted analyses to collect data on particular locations, often providing comprehensive chemical snapshots of a region or event (ACCLIP, CalNex, AEROMMA, FIREX-AQ, ATom, etc.).[8, 9]

One approach to more targeted and granular measurements are frequent measurements from mobile platforms (e.g., instrumented vans or cars). Vehicles with sampling and online measurement equipment can provide high frequency ($\sim$1 s) measurements for many species at once. Recent innovations come from driving repeatedly in the same region to provide sufficient statistics to gather a representative sample for each location. These campaigns may target a specific location, driving near a suspect emission source to capture downwind enhancements,[10–12] or might instead cover a city or region by driving down each road to create a street-level map of concentrations.[13–15] These mapping campaigns provide rich datasets that are particularly useful at identifying hyperlocal pollutant anomalies and identifying unique sources. However, due to the costs of these campaigns, they are often limited in scope (e.g., no driving at night) and persist over very short time periods.

Long-term measurements of atmospheric composition are often made by spatially sparse stationary networks (TCCON, AERONET, Pandora, ASCENT, IMPROVE, CASTNET, etc.).[16–21] These networks use both remote sensing and in situ online and offline measurements to understand the composition of the atmosphere at a specific site. These measurement sites provide robust datasets spanning long timescales, often years to decades of continual measurements. However, the capital and operational costs for these sites prohibits wide-scale

deployment, with networks often being limited to dozens of sites across continents or the whole globe. In the U.S., the densest of such networks is the U.S. Environmental Protection Agency's (EPA) Air Quality System (AQS).[22] The EPA AQS system is run by state and local governments to meet federal requirements for the monitoring of criteria air pollutants. Most sites make hourly or daily measurements of a subsample of the criteria pollutants: CO, NO, NO_2, O_3, and/or $PM_{2.5}$. However, even in densely populated areas like the San Francisco Bay Area, these sites are sparsely located (Figure 1.1) and lack the measurement capability to study air quality beyond regional and seasonal trends. Additionally, these sites lack any measurements of greenhouse gases.

Low-cost, dense sensor networks fill a niche measurement gap in our current observing system. Their reduced cost enables the deployment of sensors at high spatial densities while also making frequent ($\sim$1 min) measurements over long deployment (multiple year) timescales. This creates a dataset with the spatial density to differentiate neighborhood-scale changes in concentrations, the temporal frequency to detect transient plumes and events, and the long-term stability to evaluate seasonal and annual changes and trends in the emissions landscape. Low-cost sensor networks, particularly those focused on air quality, have become more common over the past decade.[23] Most analysis has been focused on ambient monitoring, population exposure, and public health. I believe these rich datasets can provide a wealth of information informing our understanding of urban air, particularly in understanding emission sources, patterns, and trends.

1.3 A BEACO$_2$N of Hope

The Cohen Lab at UC Berkeley has established the Berkeley Environmental Air-quality and CO_2 Network (BEACO$_2$N), a dense sensor network of low-cost air quality sensors (measuring CO, NO, NO_2, O_3, and $PM_{2.5}$) and a mid-cost CO_2 sensor.[24] All sensors are placed inside a compact enclosure which allows for simple deployment in the field (Figure 1.1). The low cost and ease of deployment for the sensor package allows for dense deployment of the sensors across urban areas. In the San Francisco Bay Area of California, there are currently 56 BEACO$_2$N sites in the field, situated with approximately 2 km spacing (Figure 1.1). The sensors are primarily deployed on the rooftops of schools, with others situated on government buildings, community centers, museums, and other buildings. One BEACO$_2$N site is at the Richmond Field Station which houses several high precision reference instruments, and three BEACO$_2$N sites are co-located with EPA AQS sites, allowing for calibrations and performance checks on the sensors. In collaboration with research groups across the globe, BEACO$_2$N sensor networks have been established in several other cities, including Los Angeles, CA; Providence, RI; Glasgow, Scotland; and Heidelberg, Germany. The work in this dissertation focuses on the network deployed in the Bay Area.

In this dissertation, I use data from the BEACO$_2$N network to demonstrate the unique insight that dense sensor networks can bring to our understanding of urban emissions. Pollutant plumes, specifically those from point sources, tend to produce sharp concentration

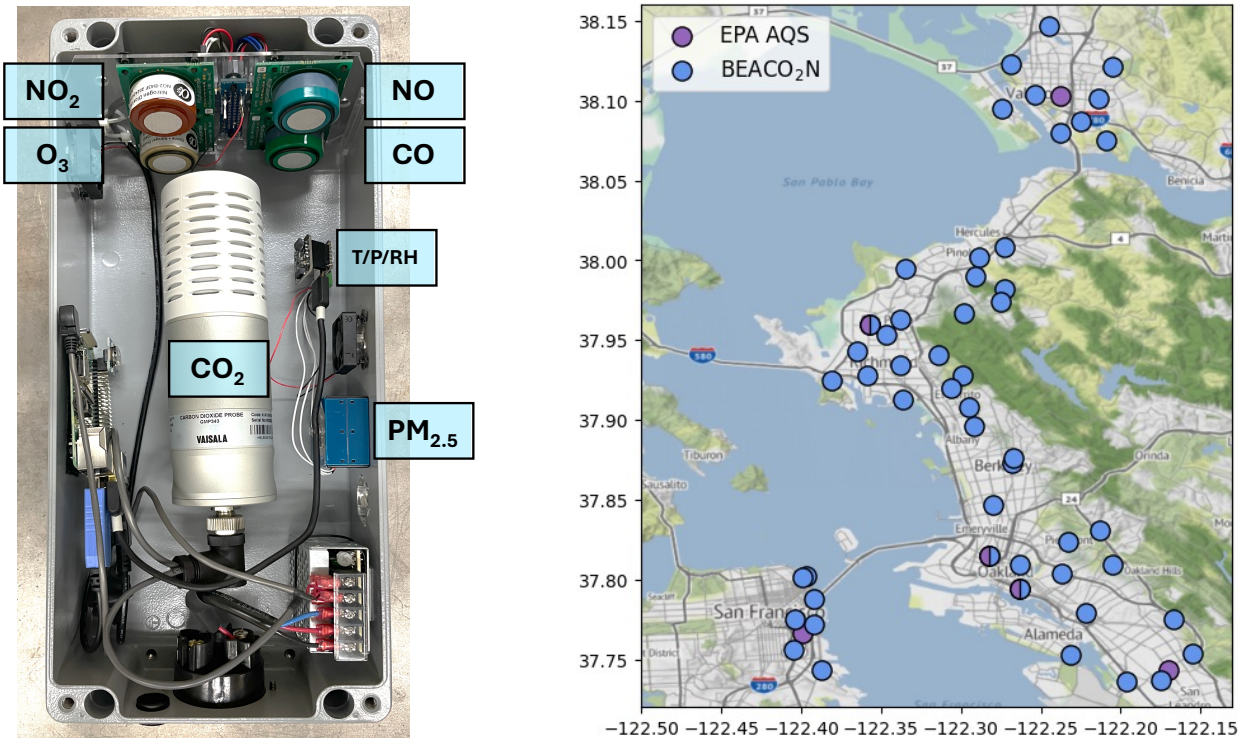

Figure 1.1: (left) Image of the $BEACO_2N$ sensor package and enclosure, with sensors labeled by the species being measured (T/P/RH corresponding to temperature, pressure, and relative humidity), and (right) a map of the $BEACO_2N$ network sites and EPA AQS sites in the San Francisco Bay Area.

gradients, while enhancement spatial patterns are highly variable due to their strong dependence on wind fluctuations. Regulatory monitoring sites like the EPA AQS network are sparsely located and report hourly averaged values, making them largely blind to local plume structures. Satellite retrievals often have too coarse a resolution to discern details about single source emission plumes, and those that do have sufficient spatial resolution suffer from infrequent revisit times, limiting the times and frequency of measurement. Thus, dense sensor networks are uniquely positioned to study small-scale and transient pollutant plumes that are easily missed or mischaracterized by other measurement platforms and techniques. Additionally, by measuring both air pollutants and CO_2, $BEACO_2N$ ambient observations can provide insights into the processes behind emissions (for example by deriving emission factors). In the following chapters, I use $BEACO_2N$ observations to constrain emissions of air pollutants and CO_2 from both transient and continuous point source emission events in the Bay Area and establish the limits to which these methods can be applied.

1.4 Summary of Chapters

One of the challenges of using low-cost sensors is devising appropriate calibration schemes that produce robust datasets with minimal uncertainty and biases. In Chapter 2, I devise a time-evolving calibration method for the Plantower PMS5003 $PM_{2.5}$ mass concentration measurements for ambient air quality conditions. I use 2 years of measurements from $BEACO_2N$ sensors deployed in the San Francisco Bay Area and Los Angeles in our analysis. The calibration uses a hygroscopic growth correction factor derived from κ-Köhler theory, in which the calibration parameters are determined empirically using EPA AQS reference data at co-located sites during the period 2021–2022. The parameters are found to vary cyclically through the seasons, and the seasonal cycles match changes in sulfate and elemental carbon PM composition fractions throughout the year. In both regions, the seasonal RH dependence calibration performs better than the uncalibrated data and the data calibrated with the EPA's national Plantower calibration algorithm. In the San Francisco Bay Area, the seasonal RH dependence calibration reduces the root mean square error (RMSE) by 40% from the uncalibrated data and maintains a mean bias much smaller than the EPA national calibration scheme (-0.90 vs -2.73 µg m^{-3}). I also find that calibration parameters forecasted beyond those fit with the EPA reference data continue to outperform the uncalibrated data and the EPA calibration data, enabling real-time application of the calibration scheme even in the absence of reference data.

In Chapter 3, I explore the ability to use dense sensor network data to analyze transient pollution events. Here, I use $BEACO_2N$ to quantify the air pollutant ($PM_{2.5}$, CO, NO_x) and CO_2 emissions from an urban fire in Albany, CA. Pollutant enhancements are measured at multiple sites, and the ensemble of observations are fit to a 2-D Gaussian model to characterize the extent of dilution prior to observation and derive emissions at the location of the fire. Consistency of the ratios at multiple locations downwind of the fire supports the precision of the network. I find that the fire emitted approximately 770 ± 30 kg of $PM_{2.5}$, 70,000 ± 20,000 kg of CO_2, 2,500 ± 300 kg of CO, and 28 ± 9 kg of NO_x. The emission ratios were found to be in the range of typical wildland fires. Using this case study, I explore the minimum plume emissions that could be observed and quantified by the network and define limits of detection and quantification.

In Chapter 4, I assess the ability to use dense sensor network data to quantify emission rates from continuous point source emitters. I use the $BEACO_2N$ observations to constrain CO_2 and air pollutant emissions from an oil refinery in the city of Richmond, CA. I identify 266 plumes crossing one or more sites in the $BEACO_2N$ network during 2022-2023 as having a source at the refinery and quantify CO_2 emissions using the Gaussian plume model. The refinery is modeled as two point sources, and total CO_2 emissions are found to be 61.3 ± 6.3 kg s^{-1}, in close agreement with the EPA FLIGHT inventory and Carbon Mapper measurements. Plume composition was found to vary, with CO/CO_2 enhancement ratios ranging from 0–5 ppb/ppm. Taking the average CO/CO_2 ratio, CO emissions are estimated to be roughly 3,000 metric tons (mt) per year, a sizable amount compared to the city's estimated non-refinery CO emissions of 6,800 mt. I show that dense monitoring networks

such as $BEACO_2N$ provide a unique resource for point source emissions quantification with broad application to plumes of varying size and composition, and I provide recommendations for future applications.

I conclude with a summary of the scope and limits of point source emission quantification by the $BEACO_2N$ network and offer discussion on future applications of these methods for analyzing emissions from ships in the Bay Area.

Chapter 2

Towards a hygroscopic growth calibration for low-cost $PM_{2.5}$ sensors

This chapter was adapted from: Patel, M. Y.; Vannucci, P. F.; Kim, J.; Berelson, W. M.; Cohen, R. C. Towards a hygroscopic growth calibration for low-cost $PM_{2.5}$ sensors. *Atmos. Meas. Tech.* **2024**, *17*, 1051-1060.

2.1 Introduction

Particulate matter (PM) is a major air pollutant, presenting a significant human health concern. $PM_{2.5}$, particulate matter with diameters less than 2.5 µm, has been linked with a number of health outcomes including decreased lung function, premature death, cardiovascular diseases, and cancer.[25, 26] As such, local PM observations are an essential part of a system for monitoring and improving community health and well-being. Additionally, coincident measurements of PM and other pollutants, like CO or NO_x ($NO_x \equiv NO+NO_2$), can be used to elicit information on urban emissions and atmospheric processes.[27] The increasing availability of low-cost PM sensors has facilitated high-density PM monitoring and widespread use outside the scientific and professional air quality communities.

A well-documented issue with low-cost nephelometric PM sensors is their size-dependent sensitivity and sensitivity dependent on the index of refraction. These sensors are imperfect nephelometers. They are most sensitive to submicron particles, and their sensitivity decreases as particles get larger with near-zero detection for particles larger than 2 µm and lower efficiency below 300 nm.[28–30] For a constant particle size distribution and composition, a single scale factor can translate the observations to those made with instruments that capture the mass of the entire size distribution. However, fixed calibrations are inadequate for temporally evolving particle size and composition distributions. One of the major drivers of variability in particle size distributions is hygroscopic growth, which is the uptake of atmospheric water onto PM. While reference instruments such as those used in the US Environmental Protection Agency's Air Quality System (EPA AQS) measure particles

under controlled, low-humidity conditions, low-cost sensors usually measure particles under ambient atmospheric conditions.[31, 32] Fluctuations in the relative humidity (RH) change particle size and refractive index through water uptake, both of which impact particle light scattering and subsequent detection by nephelometers.[33–35] On longer timescales, PM size distributions and composition vary depending on primary emissions sources and secondary PM formation pathways.[36–38] Theoretical calculations show that relative humidity is the largest source of uncertainty for optical particle sensors when the aerosol is hygroscopic.[39] An efficient calibration scheme for nephelometric sensors must therefore account for both rapid (hourly) size fluctuations due to changes in humidity and long-term (monthly) variations in particle composition and hygroscopicity.

Several previous studies have reported calibrations to correct for the hygroscopic growth of particles measured with low-cost optical sensors. Crilley et al. noted the high bias of $PM_{2.5}$ mass concentrations from optical particle counters (OPCs) when the relative humidity was high and used a bias correction scheme derived from κ-Köhler theory, which has subsequently been applied to other low-cost OPC studies.[40, 41] Similar bias correction schemes have also been applied to nephelometric PM sensors. Malings et al. used a hygroscopic growth correction on Plantower PMS5003 in the PurpleAir sensors as well as the Met-One NPM during a field study in Pittsburgh, PA, where separate parameters were set for summer, winter, and transition months to account for seasonal changes in the hygroscopicity of the particles based on measured speciation data.[42]

Malings et al. recognized the need for seasonally variant parameterization of hygroscopic growth and implemented a piecewise change in hygroscopic growth parameters to account for these seasonal changes. Here, we propose a calibration scheme for the Plantower PMS5003, a low-cost nephelometric PM sensor, whose hygroscopic growth parameters smoothly evolve through the seasons based on smooth evolution of observed composition to represent gradual changes in PM hygroscopicity over time. The Plantower is a widely used low-cost PM sensor,[29, 37, 43–45] so the development of regional, easy-to-implement corrections for these instruments is useful to air quality monitoring broadly.

2.2 Methods

The Berkeley Environmental Air-quality and CO_2 Network ($BEACO_2N$) is a high-density network of low-cost sensors spread across multiple urban centers around the globe, monitoring CO_2, CO, NO_x, O_3, and $PM_{2.5}$.[24] There are currently 57 active $BEACO_2N$ sites in the San Francisco Bay Area, with additional networks in Los Angeles, CA, Providence, RI, and Glasgow, UK. Each $BEACO_2N$ node enclosure contains a Plantower PMS5003[46] for PM measurements as well as an Adafruit BME280[47] for temperature, pressure, and humidity measurements, with fans on either end of the enclosure to cycle air through the node. The Plantower PMS5003 is a nephelometric PM sensor reporting mass concentrations for PM_1, $PM_{2.5}$, and PM_{10}, though for the remainder of this work we will only discuss the $PM_{2.5}$ output measurement for this sensor. The sensor has internal calibrations, unknown

to the user, that convert from scattered light intensity to PM mass concentrations. Here, we use the CF = ATM sensor output, which is recommended for outdoor $PM_{2.5}$ measurements. The calibration factor described herein is applied to this $PM_{2.5}$ mass concentration sensor output. Plantower data was recorded every 8 seconds and averaged to hourly data points, which are used in this analysis.

The humidity-dependent equilibrium water uptake by particles is often parametrized by the hygroscopic growth parameter, κ, which is dependent on particle composition. κ–Köhler theory can be used to derive an RH-dependent factor to account for hygroscopic particle growth.[33, 40, 43] This can be supplemented by an additional scaling factor, m, which can account for discrepancies between the assumed particle size distribution in the factory calibration and the true particle size distribution for the particles being measured.[39, 42] This leads to the following calibration algorithm:

$$PM_{2.5} = PM_{plantower} * \frac{m}{1 + \frac{\kappa}{100/RH - 1}} \tag{2.1}$$

which has two parameters, m and κ. For a given particle, κ can be calculated as the weighted average of the hygroscopic growth parameters for all constituents in the particle.[33] Similarly, one could use the weighted average of this value over a sample of particles to get their collective growth parameter. Since composition information for PM is not as widely available as total $PM_{2.5}$ mass concentration measurements, we determine κ and m empirically and validate their values over time using seasonal trends in observed PM composition. This empirical approach is more accessible to anyone trying to implement this calibration on sensors in areas with limited speciation data. However, as a point of comparison, we also calculate κ using data from the EPA AQS Chemical Speciation Network. κ values for the major aerosol components are taken from various studies in the literature.[33, 48, 49]

The empirical parameters m and κ in Eq. 2.1 are calculated using co-located $BEACO_2N$ Plantower PMS5003 and EPA AQS sites, where the EPA AQS $PM_{2.5}$ provides a reference concentration for the calibration (Table 2.1). The fitting was performed on hourly Plantower and RH data with the Python package scipy.optimize.[50] We describe application and evaluation of this calibration approach to the $BEACO_2N$ networks in the San Francisco Bay Area and Los Angeles, CA during the years 2021 and 2022. A summary of the datasets used can be found in Table A.1.

In the San Francisco Bay Area, we utilize two co-location sites in the 2021–2022 period of study. These are listed in Table 2.1 along with a co-location site in Los Angeles, CA. Note that the Castelar ES site is located 1.06 km from EPA site 06-037-1103, whereas the two Bay Area $BEACO_2N$ sites are on-site with their respective EPA AQS reference instruments. All three EPA AQS sites measured hourly $PM_{2.5}$ using a Met One BAM-1020 Mass Monitor w/VSCC.

The EPA has also developed a national Plantower calibration algorithm with the following form:

$$PM_{2.5} = 0.524 * PM_{plantower} - 0.0862 * RH + 5.75 \tag{2.2}$$

Table 2.1: Co-location sites used in this study

$BEACO_2N$ Site	Region	Co-Located EPA Site	Nearest AQS CSN Site
Laney	Bay Area, CA	06-001-0012	06-085-0005
EBMUD	Bay Area, CA	06-001-0011	06-085-0005
Castelar ES	Los Angeles, CA	06-037-1103	06-037-1103

which they currently apply to PurpleAir Plantower PMS5003 measurements on their AirNow website.[44] This scheme, herein the "National EPA Calibration", is used throughout the paper as a point of comparison.

2.3 Results and Discussion

RH Calibration

Figure 2.1 a and b show the calibration coefficients generated by fitting the observations from the Laney site (Table 2.1) Plantower sensor to the EPA reference data using a 4-week moving window. A strong seasonal cycle is evident. The EPA AQS Chemical Speciation Network (CSN) (sites used are listed in Table 2.1) provides measurements for components of PM, including the major aerosol species: ammonium, nitrates, sulfates, organic carbon, and elemental carbon (EC). Figure 2.1 c and d show the sulfate and elemental carbon (EC) fraction observed at the CSN site nearest to Laney. Sulfate is the most hygroscopic of the major components of aerosols, while EC is not hygroscopic.[33, 51] For this reason, we will use these species to infer trends on the overall hygroscopicity of $PM_{2.5}$ across the seasons.

The speciation data from the nearest CSN site shows strong seasonal trends where the sulfate fraction is highest in the summers while the EC fraction is highest in the winters. The fitted κ values show an appropriate response, where the particles are most sensitive to RH in the summers and least sensitive in the winters. The scaling factor, m, follows the same seasonal cycle as κ. This can be reasoned by concluding that when κ is large, particles are subject to more hygroscopic growth, and consequently particle size distributions are shifted to larger sizes which are detected with less efficiency by the Plantower sensor. Since κ and m are calculated empirically, they may also respond to factors besides hygroscopic growth, which could account for differences seen between trends in these parameters and trends in the displayed aerosol components. Using the EPA AQS CSN data for all major aerosol components, we construct κ from the speciation data and compare it to the empirically derived κ in Figure A.1. We find reasonably strong agreement in the seasonal trend for the two κ timeseries, with peaks in κ occurring during the same times of the year.

The calibration coefficients can be smoothed, preventing overfitting, by fitting the coefficients to a sine curve. The gray lines in Fig. 2.1 show the sine curve fits for 2021 and 2022, where the periods of the curves are set to 1 year. Parameters for the sinusoidal fits can be

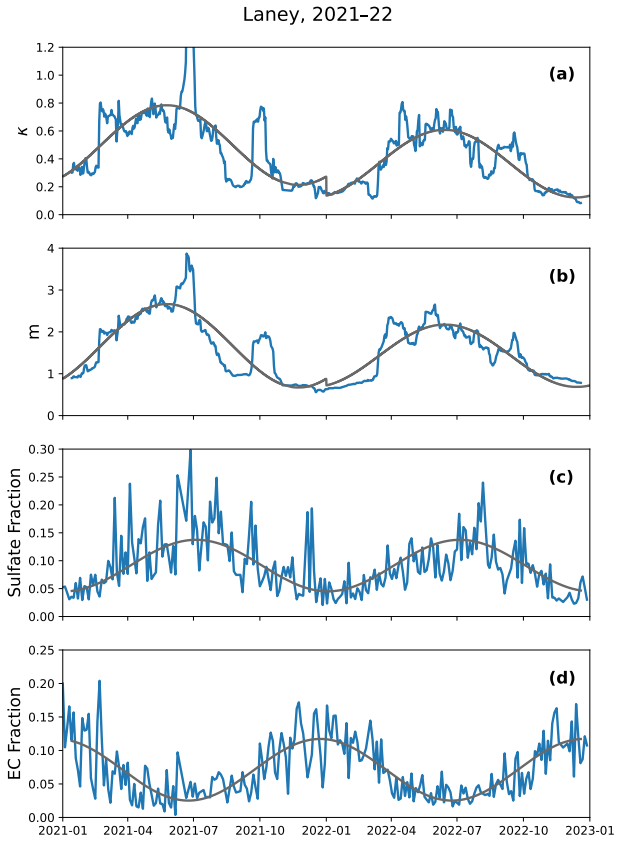

Figure 2.1: (a,b) Calibration parameters generated for Laney site, and (c,d) particle speciation data from the nearest EPA AQS CSN site.

found in Table A.2. Application of Eq. 2.1 using these smoothed κ and m parameters is herein referred to as the "Seasonal RH Dependence Calibration". This calibration is applied to the data over 2021 and 2022. Figure 2.2 shows a timeseries of the pre- and post-calibration sensor data, along with the EPA AQS reference measurements. Table A.3 shows that the calibrated data has a significantly improved Pearson's correlation, r, and NRMSE, especially during the winter months.

Evaluation

Figure 2.3 shows that the strong RH-dependent bias in Plantower PMS5003 outputs is removed through the implementation of the seasonal RH dependence calibration scheme. Notably, the national EPA calibration scheme, which assumes a linear RH-dependence, does not properly account for the non-linear RH effects on particle size and detection. Figure A.2 shows that the seasonal RH dependence calibration also removes the temperature dependence

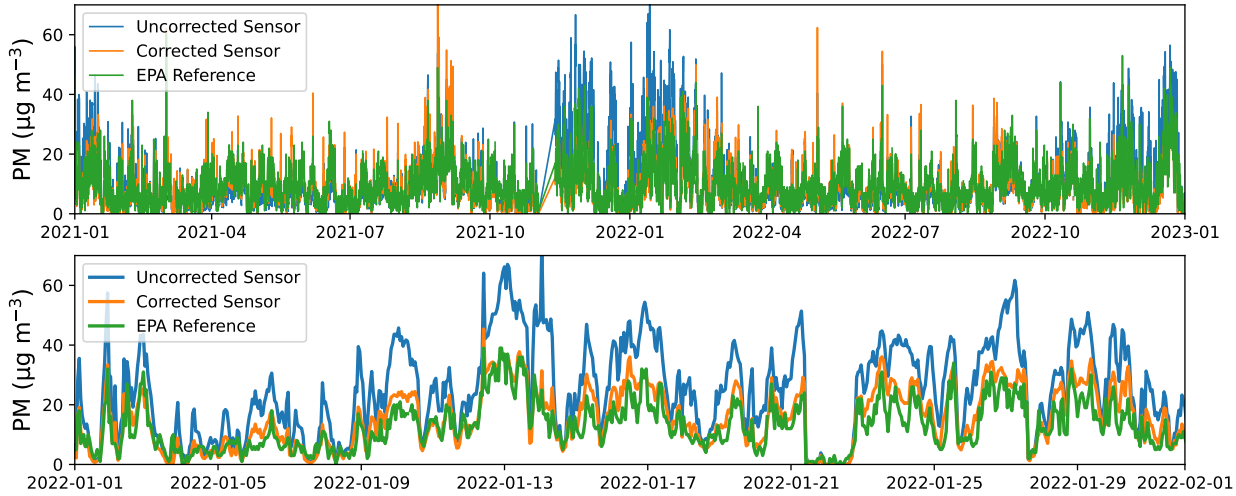

Figure 2.2: Timeseries of the Laney site Plantower $PM_{2.5}$ data without and with the seasonal RH dependence calibration, compared to the co-located EPA $PM_{2.5}$ reference data for the whole two year study period (top) and for the subset of January 2022 (bottom).

of the residuals. This was expected since most of the temperature dependence was likely due to covariance of temperature and RH rather than intrinsic temperature effects on sensor measurement or performance. Figure 2.4 shows the uncalibrated and calibrated Plantower measurements compared to the EPA AQS reference observations for the entire two-year period. Both the National EPA calibration and the seasonal RH dependence calibration led to reductions of ∼40% in the RMSE and increases of ∼0.75 in the coefficient of determination (R^2), but the EPA national calibration introduces a large negative bias in the measurement. It is worth noting the importance of having κ and m change through time. When the calibration is applied with an optimized but constant κ and m parameter (κ = 0.311, m = 1.02), the performance of the calibration is sizably worse (R^2 = 0.407, RMSE = 4.884 µg m^{-3}, Mean Bias = -2.296 µg m^{-3}) than the seasonal RH dependence calibration, as apparent in Figure A.3.

There were no major smoke events or other air quality events of substantial nature (e.g. multiday events, significantly high PM concentrations, etc.) during the 2021-2022 study period in the Bay Area. In August and September of 2021, there are many days with air quality warnings for smog due to winds carrying smoke from nearby fires and high temperature events worsening local pollution. If we remove data during this time period from Fig 2.4, the figure is virtually unchanged and the statistics are quite similar (Fig. A.4). In other time periods, we'd expect that significant air quality events could impact the analysis and should be removed from the dataset prior to fitting and applying the calibration.

Analyzing the distribution of errors from each of the calibration types under different mass concentration and humidity levels can help assess the completeness of each of the

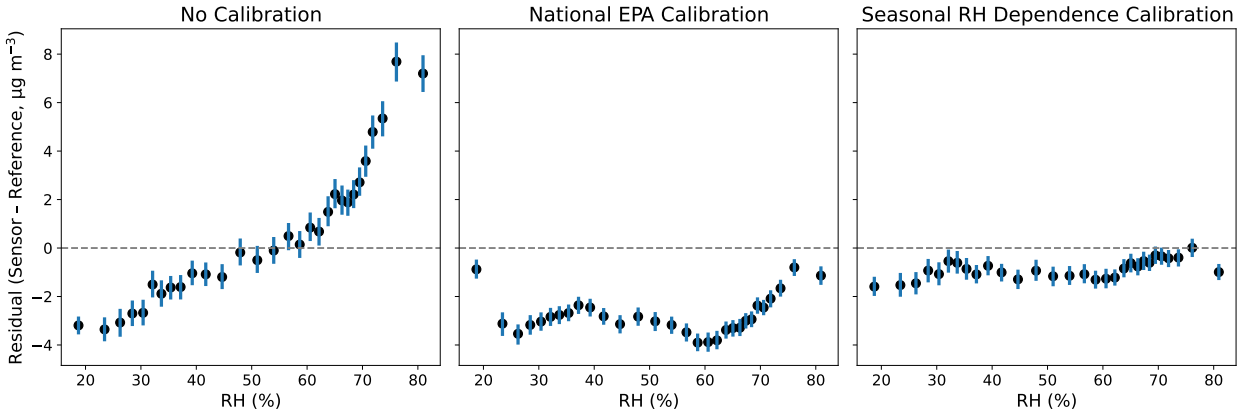

Figure 2.3: Measurement residuals (sensor output – EPA AQS values) for data from the Laney site with different calibration algorithms, binned into 30 RH bins.

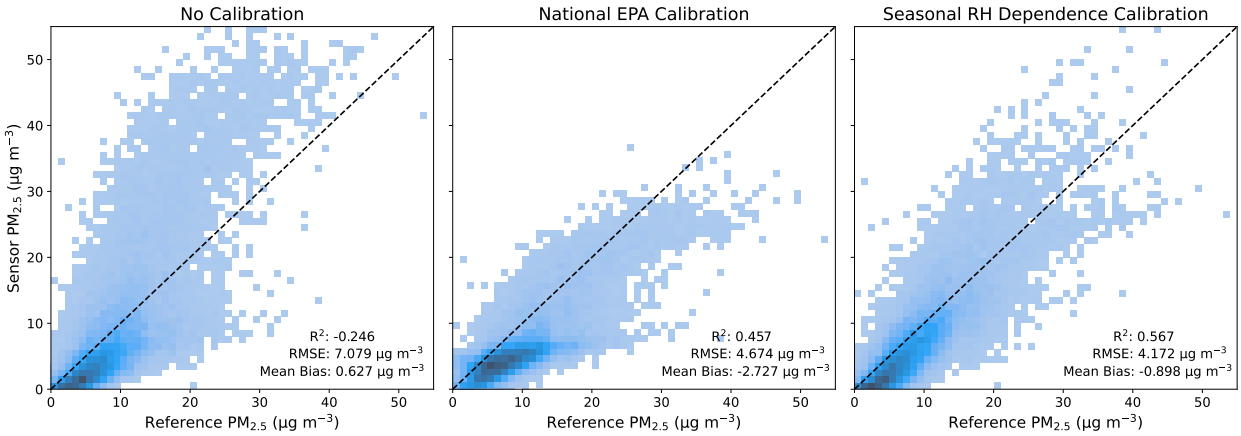

Figure 2.4: Sensor predicted $PM_{2.5}$ values versus EPA reference values for Laney site from 2021–2022 with different correction algorithms. Performance metrics are the Coefficient of Determination (R^2), root-mean-square error (RMSE), and mean bias.

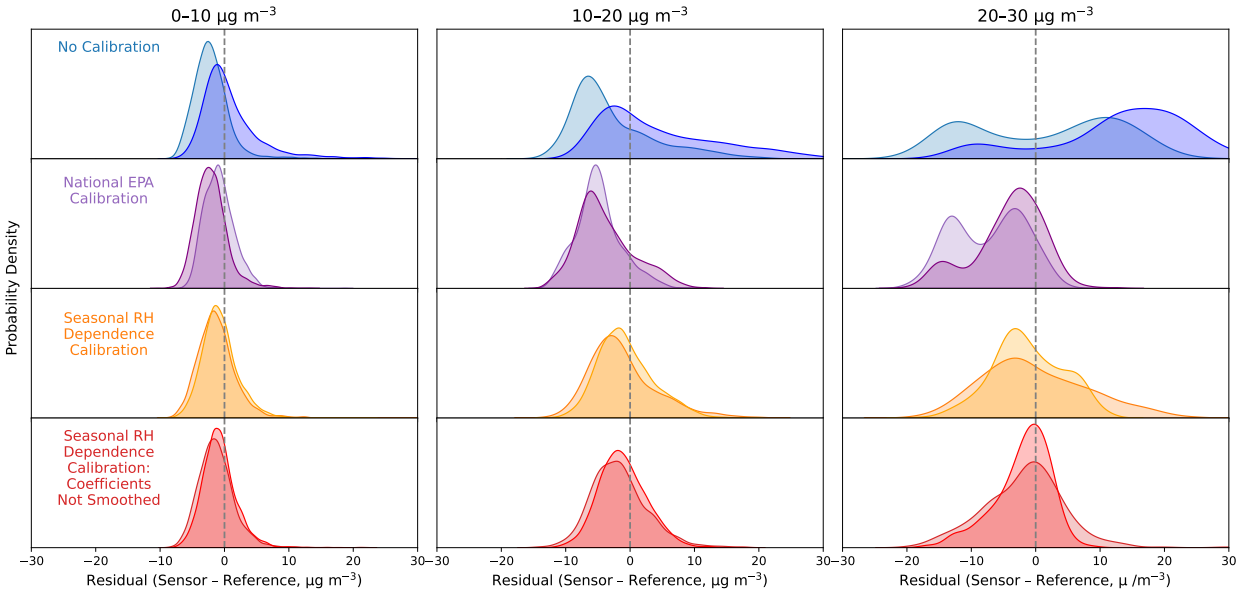

Figure 2.5: Sensor residual distributions for different calibration schemes at different $PM_{2.5}$ mass concentration bins for RH $< 50\%$ (light color) and RH $> 50\%$ (dark color) conditions. The calibration scheme "Seasonal RH Dependence Calibration: Coefficients Not Smoothed" uses the calculated κ and m values as-is, without smoothing to a sine wave.

calibration schemes. We would expect that a complete calibration would produce zero-centered, Gaussian error distributions since all remaining errors would be from random noise in the measurement. Looking at the distribution of errors at different $PM_{2.5}$ mass concentrations (Fig. 2.5) it is evident that, while the seasonal RH dependence calibration produces errors more symmetric and centered near zero than the uncalibrated data and the EPA calibration data, the errors are still not perfectly Gaussian, especially when the $PM_{2.5}$ mass is high. This suggests that there are other processes and aerosol properties at play unaccounted for by this calibration, as discussed further below. We also explore the error distributions when κ and m are not smoothed to sine waves and find no meaningful differences between the smoothed and unsmoothed cases when $PM_{2.5} \leq 20$ µg m^{-3}, which accounts for over 95% of the data (Fig. 2.5). As such, representing seasonal changes of κ and m throughout the year as sine waves is a valid approximation.

Inter-region and intra-region comparisons

Given that the κ and m parameters follow trends consistent with PM speciation data, it is reasonable to assume that the parameters generated at one site can be applied to nearby sites if the particle composition is homogenous across the urban area.

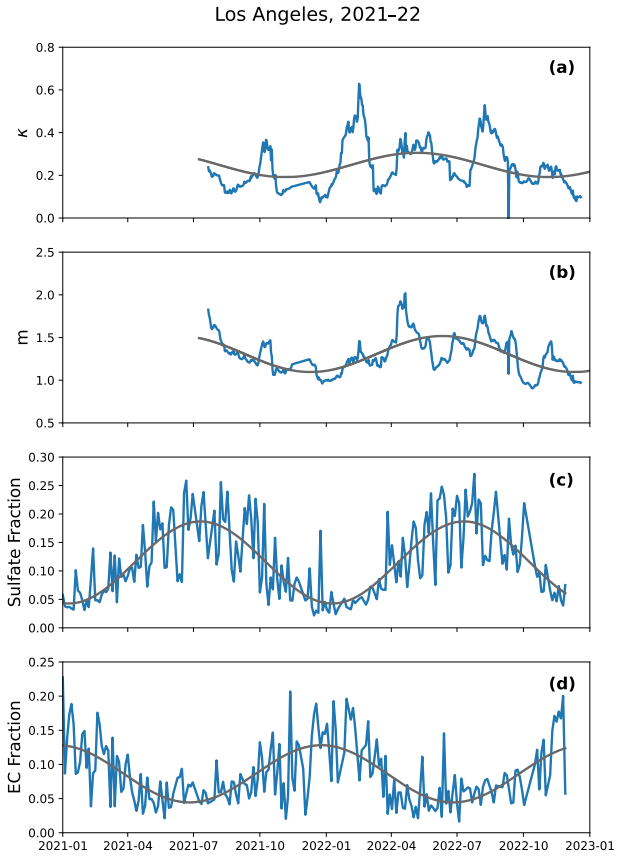

Figure 2.6: (a,b) Calibration parameters generated for the Los Angeles site, and (c,d) particle speciation data from the nearest EPA AQS CSN site.

To further test this assumption, we independently generate calibration coefficients for another Bay Area co-location pair at the EBMUD site (Table 2.1). As seen in Fig. A.5, the EBMUD and Laney co-location pairs independently reproduce nearly identical calibration coefficients, ensuring that the coefficients are not over-fit on one site but rather reflect regional trends in PM composition. Another concern is the possibility that individual sensors have disparate sensitivities or offsets. We find that uncalibrated measurements from 17 co-located Plantowers show strong agreement with each other (Fig. A.6), with differences between sensors generally less than 1 µg m^{-3}, suggesting that there is little sensor-to-sensor variability in sensor performance.

The seasonal RH dependence calibration scheme was tested in another urban area to ensure its generalizability beyond the Bay Area. Using a co-location site in Los Angeles, CA, we find that the aerosol composition again displays seasonality (Fig. 2.6), with the sulfate fraction highest in the summers and the EC fraction highest in the winters. In Los Angeles, as in the Bay Area, the trends in κ and m match the composition variations. κ

and m are largest in the summers when the particles are the most hygroscopic, and smallest in the winters when the particles are the least hygroscopic. The κ sine fitting has a sizable phase shift from the fits of the particle composition data, though this might be attributable to the low quality of the sine fitting for the LA data (Table A.4). Additionally, there is poorer agreement between this empirical κ and the composition-derived κ (Fig. A.7). This could indicate that in Los Angeles, factors unrelated to hygroscopicity are being captured in the empirical calculation of κ. These factors could include sub-seasonal changes in refractive index or particle size distribution, though further study is needed to provide evidence for these. Despite this, the seasonal RH dependence calibration outperforms the national EPA calibration and the uncalibrated data, with a higher coefficient of determination and lower RMSE (Table A.5).

Real-time application of the calibration

Since the calibration coefficients generated in Fig. 2.1 and Fig. 2.6 are periodic and aerosol composition and its seasonal variation are changing slowly from year to year, it is possible to apply the seasonal RH dependence calibration to sensor measurements in real-time without the need for EPA reference measurements to be real-time as well. We test the validity of this approach by generating sinusoidal calibration coefficients in 2021 and projecting them forward 6 months into 2022 without using the 2022 reference data, as shown for data at the Laney site in Fig. 2.7. Like before, both the seasonal RH dependence calibration and the national EPA calibration led to significant reductions in the RMSE ($\sim$40%), and the national EPA calibration produces a significant negative bias (–2.39 µg/m^3, compared to 0.98 µg/m^3 in the seasonal RH dependence calibration). Thus, in regions with strong and stable seasonal cycles for PM composition, the sinusoidal parameters can be applied in the months following the period in which they were generated with reasonable accuracy.

Limitations of the Calibration

There are several limitations worth noting in this calibration scheme. First, the calibration focuses on discrepancies arising from hygroscopic growth of particles, and while theoretical calculations show this to be the largest source of error,[39] there are several other documented sources of error. Changes in the particle size distribution unrelated to hygroscopic growth, such as from changes in the sources of PM, are partially accounted for by the m parameter, but this is likely incomplete. Changes in particle composition also change the refractive index of the particles, which is ignored by this correction scheme.

Additionally, the method assumes that particle composition is uniform across the domain and changes slowly and smoothly over the course of a year to reflect seasonal changes in particle size and composition. As such, non-seasonal changes in particle size and hygroscopicity are not properly corrected by this method. Isolated extreme events require unique corrections, as is the case when measuring wildfire smoke or dust events.[52, 53] Sensors that are close to unique point sources might be consistently subject to particulate matter

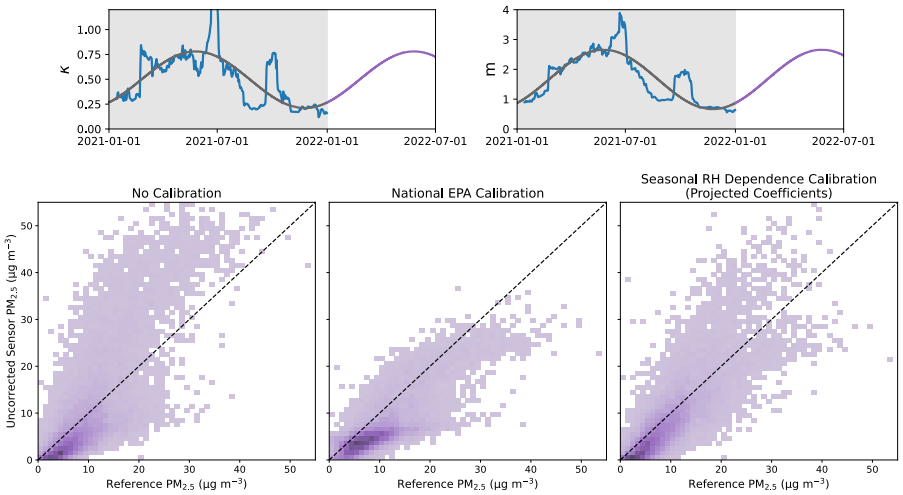

Figure 2.7: (top) κ and m parameters calculated at the Laney co-location site in 2021 with sinusoidal fits projected 6 months into 2022, and (bottom) sensor predicted $PM_{2.5}$ values versus co-located EPA reference values for the Laney site for Jan–Jun 2022 with different calibration algorithms.

of a different composition and size distribution than other sensors in the network and may subsequently experience systematic biases.

There are also potential errors associated with slow drift that can occur over multiple years. Due to changes in PM sources and relative source loadings, PM composition is not expected to be the same year-over-year, so periodic recalculation of the coefficients is likely necessary. If one sensor in a network is permanently co-located with a regulatory instrument, it can be used to update the coefficients year to year for all sensors within its region. Though sensors can drift and degrade over time, current literature finds that these sensors tend to be stable for at least 3 years.[54]

2.4 Conclusions

The Plantower seasonal RH dependence calibration is aimed at addressing biases in sensor measurement caused by changes in the size distribution of PM, largely from fluctuations in relative humidity leading to hygroscopic growth and seasonal changes in particle composition that affect hygroscopicity. We provide a physically meaningful calibration scheme that is simple to define and implement for multiple regions in the United States. The seasonal RH dependence calibration utilizes only RH as an additional parameter and has calibration coefficients that reflect seasonal changes in PM speciation. This method provides a time-variant calibration scheme that can be implemented in real-time due to the periodic

nature of the calibration coefficients. Speciation data provides insight and validation to the calibration parameters but is not needed in creating the calibration. Additionally, analysis of multiple co-location pairs in the Bay Area show that the calibration parameters are generally uniform within a given region, and as such this calibration can be generated for many sites using limited co-location pairs if there is reasonable confidence that aerosol speciation is uniform across the application area. Future work will be done to explore the stability of this calibration over long periods of time and work towards simple methods for correcting the unaccounted errors mentioned in the limitations section of the discussion.

The seasonal RH dependence calibration is being actively applied to the $PM_{2.5}$ measurements in the $BEACO_2N$ network, which are publicly available and can be found on their website (beacon.berkeley.edu).

Chapter 3

Plume Detection and Emissions Quantification Potential Using a Dense Sensor Network

This chapter was adapted from: Patel, M. Y.; Zhu, Y.; Winter, A. R.; Asimow, N. G.; Cohen, R. C. Plume Detection and Emissions Quantification Potential Using a Dense Sensor Network. *ACS EST Air* **2025**, *2*, 1099-1106.

3.1 Introduction

Low-cost sensor (LCS) networks have rapidly increased in popularity in the last decade, providing high spatial and temporal resolution measurements of critical pollutants and greenhouse gases (GHGs).[23, 55, 56] A primary benefit of densely spaced monitoring networks is the ability to capture small-scale variations in air composition.[57–62] The heterogeneous landscape of urban spaces leads to hyperlocal variability in pollutant and GHG concentrations, which can easily be missed by sparse regulatory monitors and coarse remote sensing products. These fine-scale variations are an important component in determining air pollution exposure and disparities.[63–67] One source of this heterogeneity is small-spatial scale and episodic emission events from point sources such as urban fires or construction sites, mobile sources, or continuous emissions from industrial stacks. Acute exposure to high pollution events can have serious health consequences.[68–72] For example, studies have shown that people exposed to the emission plumes of oil and gas flaring and industrial releases are subject to serious negative health consequences, including respiratory diseases and impaired fetal development.[73, 74] Additionally, events like house fires and industrial flaring or accidents are unaccounted for in inventories and models due to their intermittent nature. Dense stationary monitoring networks can provide insight into the frequency and magnitude of events like these. LCS networks have been widely used for detection and general characterization of air pollution outcomes from a variety of events,[75–79] but emissions quantification

remains far less common. While a number of studies have used sensor networks to update and refine regional emissions estimates, for example using inverse modelling for CO_2 emissions,[80–83] to our knowledge, there are no prior studies interpreting measurements from a LCS network to quantify the emissions of a single emission event from its resultant plume. Here, we outline a methodology for plume characterization and emissions quantification from a single event using a low-cost sensor network. We describe application of the method to a specific case study, a 2022 fire in the city of Albany, CA. Using this case study, we describe the types of point sources that should be quantifiable with a $BEACO_2N$-like sensor network and discuss the factors affecting the limits of detection for plumes in this network. We also make note of the plume detection across the network as an independent confirmation of network performance for the different instruments deployed in each $BEACO_2N$ node.

3.2 Methods

$BEACO_2N$ Observations

The measurements used in this analysis are from the Berkeley Environmental Air-quality and CO_2 Network ($BEACO_2N$), which has been described extensively elsewhere.[24, 84] Briefly, $BEACO_2N$ is deployed in several cities around the globe, with about 56 sites currently in operation in the San Francisco Bay Area of California. Each sensor package measures a suite of gases and particles. Most instruments are installed on building rooftops (most often 3-10 m above ground level) at approximately 2 km spacing. CO_2 is measured at 5 s intervals using a Vaisala CARBOCAP Carbon Dioxide Probe GMP343. The CO_2 sensor calibration is described in detail in Delaria et al.[85] Briefly, the sensors have a temperature-dependent offset which is corrected for using comparisons to a reference-grade instrument. Absolute CO_2 measurements are found to have errors of less than 1.6 ppm. In this work, we focus on the short-term enhancement in CO_2 concentrations, which minimizes the effects of biases in the baseline that may persist in the measurements. CO, NO, NO_2, and O_3 are measured at 8 s intervals using the Alphasense CO-B4, NO-B4, NO2-B43F, and Ox-B431 electrochemical gas sensors. Calibration methods for these individual sensors are presented in Winter et al.[86] The calibrations account for cross-sensitivities and the influences of temperature and humidity at the sensor, as well as drifts in sensitivities and offsets over time. $PM_{2.5}$ is measured at 8 s intervals using a Plantower PMS5003 sensor. Plantower sensor performance has been shown to be sensitive to particle size, refractive index, and hygroscopicity.[39] Ambient $PM_{2.5}$ in the $BEACO_2N$ network is calibrated using the methods outlined in Patel et al.[87] However, given the distinct composition of fire smoke compared to ambient urban aerosol, unique corrections are needed to interpret the absolute $PM_{2.5}$ measurement. Several studies have found similar corrections for wildfire smoke.[53, 88, 89] Here we use a scaling factor of 0.79 from Holder et al., which was calculated for the cf=atm output of the Plantower.[53] Data were averaged at 1-minute intervals for this study.

The 2022 Albany Hill Fire

The subsequent analysis focuses on a fire at Albany Hill, an urban park in the city of Albany, CA, at approximately 37.8931°N, 122.3060°W. The fire occurred on June 26, 2022, starting sometime after 15:00 local time (PDT) with the fire department arriving at 15:27.[90] The fire, believed to be the result of arson, burned a forested area containing grasses, shrubs, and eucalyptus trees on the west side of the park.[91, 92]

Plume Characterization, Fitting, and Emissions Calculation

The timeseries at each BEACO$_2$N site was analyzed to derive concentration enhancements caused by the fire plume. Aerosol enhancements were quite large, making visual identification of the sites impacted straightforward. Outside the fire plume, ambient PM concentrations at this time were very low and consistent across the BEACO$_2$N network. The plume enhancement at each site is defined as the difference between the peak concentration measured at the site and the baseline for the site, where the baseline is a polynomial fit of the timeseries of one minute data before and after the identified plume time. The baseline was fit on 30-60 minutes of data preceding and following the plume period (Figure B.1). Using the times that a given site was impacted by the fire as determined from the PM measurements, the enhancements for CO, NO_x, and CO_2 were calculated similarly. This process is demonstrated in Figure B.1. Uncertainty in the measured enhancement is defined as the uncertainty in the baseline (the root-mean-square deviation in the baseline fit to the concentrations outside of the plume window) and the uncertainty in the peak concentration (standard deviation of the peak concentrations over 5 minutes) combined in quadrature. The time of the peak enhancement is also recorded at each site. The measured enhancement at each site shows an approximate exponential decay with respect to the time the peak enhancement is measured at the site, which is used to calculate a rate for dilution.

To calculate the total emissions from the fire event, we use a 2-D Gaussian function to model the plume. This function allows conversion of the measured enhancements and arrival times to bulk mass of pollutants. At each 1-minute timestep, the $PM_{2.5}$ enhancements at all sites were fit to the following equation:

$$G(x,y) = Ae^{-[a(x-x_o)^2+2b(x-x_o)(y-y_o)+c(y-y_o)^2]} \tag{3.1}$$

$$a = \left(\frac{cos^2\theta}{2\sigma_x^2} + \frac{sin^2\theta}{2\sigma_y^2}\right), b = \left(-\frac{sin(2\theta)}{4\sigma_x^2} + \frac{sin(2\theta)}{4\sigma_y^2}\right), c = \left(\frac{sin^2\theta}{2\sigma_x^2} + \frac{cos^2\theta}{2\sigma_y^2}\right) \tag{3.2}$$

where the concentration of the pollutant G is represented by a 2-D Gaussian plume on the x-y plane. Longitude and latitude coordinates were reprojected to the Universal Transverse Mercator (UTM) coordinate system such that x represents distance east/west of the fire origin and y represents distance north/south of the fire origin. The plume is parameterized by the following variables: A is the amplitude of the plume, x_0 and y_0 are the center of the plume, and s_x and s_y are the spread of the plume in the along-trajectory and cross-trajectory

directions, where q is the angle of trajectory at each point in time, as discussed below. All six of the above variables are expected to evolve with time. As such, this fit could be done for every timepoint to yield a set of plume parameters for each minute. However, since the plume passes over the water, where we have no observations, when travelling between Richmond, CA and Vallejo, CA, the fitting was first performed on two periods of time (16:00 – 16:30 over Richmond, and 17:00 – 17:40 over Vallejo). Then, the x_0 and y_0 positions of the plume at each timepoint were smoothed and connected to determine the full plume trajectory, including the period over the water, as shown in Figure B.2. Subsequently, q was fixed to be the angle of the trajectory in Figure B.2 at each timepoint. Now, with x_0, y_0, and q constrained, the fitting was performed again at each timepoint to yield values for A, s_x, and s_y for every minute. Since the plume is expected to smoothly evolve over time, these parameters were smoothed over time with polynomial fittings to model a realistic evolution of the plume and limit the effects of any minute-to-minute variation that might interfere with the fitting at any one timeframe. From the Gaussian fit, the bulk $PM_{2.5}$ mass could be determined by integrating over the entire Gaussian plume. The boundary layer height is estimated from NOAA's High Resolution Rapid Refresh (HRRR) model and used as vertical integration bounds, assuming a well-mixed boundary layer. From enhancement ratios of pollutants measured at the nearest measurement site to the fire source, the mass of CO_2, CO, and NO_x emitted could also be calculated. Uncertainties in the emissions mass estimates are calculated from the range of fitting parameters in the Gaussian fitting combined with the uncertainties in the measured enhancements. The Gaussian fitting, as well as the exponential decay fittings for the dilution rate calculation, were performed using the Scipy Optimize package in python.[50]

NOAA HYSPLIT Dispersion Model

As a comparison to the measured spread of the smoke plume, we used NOAA's Hybrid Single-Particle Lagrangian Integrated Trajectory (HYSPLIT) dispersion model and compared particle dilution rates. The model was run using NOAA's HRRR 3-km model as meteorological input. The release was from 0 to 50 m above ground level (AGL), with the measurement averaging layer at 0-100 m AGL. Multiple release heights were tested and produced nearly identical results. Deposition was off when running the model. $PM_{2.5}$ deposition is assumed to be negligible, as supported by the consistent $PM_{2.5}$/CO ratio across sites observed in the analysis below, as well as the short timescale (hours) being studied here compared to $PM_{2.5}$ lifetime estimates on the order of days from the literature.[93–95]

3.3 Results and Discussion

Plume Enhancements and Dilution

The peak arrival times and pollutant enhancements, defined as the difference between the measured concentrations and the baseline (the concentration expected had the plume not passed through), are listed in Table 3.1 for the sites shown in Figure B.3. The PM, CO, and CO_2 enhancements are resolvable for the whole distance in which the plume passes through the measurement domain, whereas NO_x is only resolvable close to the plume source. This is due to the size of the concentration enhancement relative to the sensor sensitivity and noise at the minute resolution.

Table 3.1: Pollutant enhancements measured at BEACO$_2$N sites where the fire plume was detected (NR: Not Resolvable)

Site	Peak Time	$\Delta PM_{2.5}$ ($\mu g/m^3$)	ΔCO (ppb)	ΔNO_x (ppb)	ΔCO (ppm)
25	16:18	185.2 ± 15.5	472.7 ± 38.3	3.42 ± 0.97	8.56 ± 1.89
23	16:21	66.5 ± 7.7	172.9 ± 15.3	NR	4.23 ± 0.93
14	16:26	72.1 ± 1.1	–	–	–
13	16:52	22.4 ± 0.9	46.0 ± 5.4	NR	NR
65	17:02	42.9 ± 2.3	129.7 ± 9.5	NR	3.48 ± 1.07
78	17:06	31.8 ± 0.8	82.2 ± 8.9	NR	4.42 ± 1.38
80	17:07	29.0 ± 0.8	65.4 ± 4.8	NR	NR
81	17:11	25.2 ± 1.0	59.7 ± 5.1	NR	NR
63	17:14	24.1 ± 1.0	52.2 ± 5.5	NR	2.38 ± 1.14
64	17:16	22.5 ± 0.9	61.5 ± 9.2	NR	2.11 ± 0.99
57	17:16	14.7 ± 0.6	37.9 ± 4.9	NR	1.86 ± 0.79
82	17:17	10.8 ± 1.1	23.5 ± 1.9	NR	NR
60	17:24	13.6 ± 0.6	42.2 ± 2.5	NR	1.25 ± 0.83
61	17:25	27.7 ± 2.3	59.6 ± 7.1	NR	1.91 ± 1.20

The PM and CO enhancements over time, as shown in Figure 3.1, show great consistency, suggesting that concentration decreases in the measured PM enhancements are driven by diffusion and mixing, rather than loss processes. We can characterize the rate of dilution from the measured enhancements and compare it to the NOAA HYSPLIT particle dispersion model. The dilution rate is calculated by fitting the maximum plume concentration across time to an exponential decay. Measured concentrations represent a lower limit to the plume maximum at the measurement time. Sites with lower concentration measurements than sites measuring the plume at a similar time are likely sampling the fringe of the plume. These sites, shown in grey in Figure 3.2, are removed from the exponential fit so that the peak plume concentration over time is better represented. For the HYSPLIT model, we fit the peak concentration at each 15-minute timestep to an exponential of the same form.

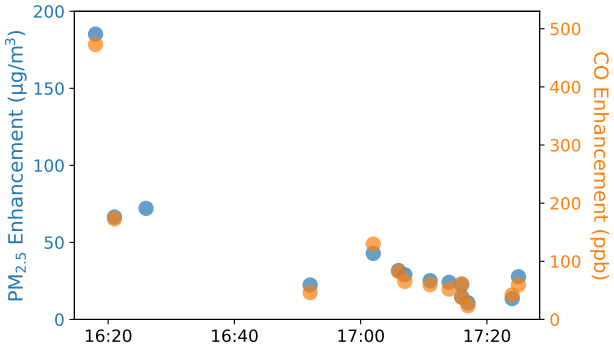

Figure 3.1: $PM_{2.5}$ and CO peak enhancements at $BEACO_2N$ sites against their peak times.

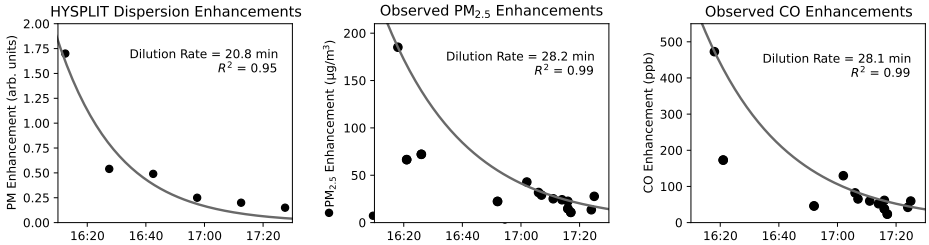

Figure 3.2: Peak concentrations over time for (a) the HYSPLIT Dispersion model plume and (b,c) observed PM and CO enhancements at the $BEACO_2N$ sites. Dilution rates are the e-folding distances for the overlaid exponential curve fits. Sites colored grey were omitted from the curve fitting.

In Figure 3.2, we show the rates of dilution for the HYSPLIT run and measured pollutant enhancements. We find them to be fairly similar in all the three cases, with the modeled dilution being slightly faster than the observed dilution. This could be related to small errors in the meteorological field, as the trajectory of the plume in the HYSPLIT model does not match to the observed plume path (Figure B.4). The dilution shows some potential of being bi-exponential, potentially indicative of a fast initial dilution from vertical mixing followed by a slower component from the horizontal plume spread. However, the data are insufficient to test this possibility. These observed dilution rates are used later on to explore the limits on plume detections in a sensor network. The relative enhancements between different species also provides useful insights to the plume event. For example, the measured CO/CO_2 enhancement ratio was 0.055 ± 0.013 ppm ppm^{-1}, indicating a combustion efficiency of about 95%. Additionally, the NO_x/CO and $PM_{2.5}/CO$ ratios are 0.007 ± 0.002 ppb ppb^{-1} and 0.39 ± 0.04 µg m^{-3} ppb^{-1}, respectively. While the NO_x/CO ratio and CO/CO_2 ratio are similar to values from the fire emission literature, the $PM_{2.5}/CO$ ratio is slightly higher than

observed for a typical wildfire, where the usual range is 0.090 – 0.350 µg m^{-3} ppb^{-1}.[96–99]

Plume Fitting and Emissions Quantification

To quantify the emissions from this fire event, we fit the measured pollutant enhancements at each timestep to a 2-D Gaussian plume as described above. In choosing a 2-D Gaussian plume, we assume that pollutant concentrations are vertically well-mixed in the boundary layer. This assumption can be tested by comparing the height of the boundary layer to vertical mixing rates. The boundary layer height during this event is estimated to be 305 m based on NOAA HRRR model outputs. Vertical mixing can be parameterized by the vertical turbulence intensity, s_z. The first site is located 3.0 km away from the fire origin. Calculating the vertical mixing by the methods of Hanna et al., s_z is estimated to be about 1900 m at a distance of 3 km.[100] So, the vertical plume spread far surpasses the boundary layer height, validating the assumption of a well-mixed boundary layer on the scales studied here.

For this assessment. $PM_{2.5}$ was used to model the plume, as it was measured at the most sites and had the most discernible baseline. As described in the methods, performing the fitting at each time stamp and smoothing the parameters allows for us to model the full plume evolution (Figure 3.3). The fitting parameters yield a calculated total mass of $PM_{2.5}$ in the plume of 770 ± 30 kg. From the relative enhancements between species, we then calculate emissions of 70,000 ± 20,000 kg for CO_2, 2,500 ± 300 kg for CO, and 28 ± 9 kg for NO_x. Based on the typical carbon content of eucalyptus trees, the site of the fire had ample biomass available to account for the quantity of CO_2 emissions estimated from this event.[101, 102]

Plume Detection Limits for a Dense Sensor Network

The above analysis shows how a densely spaced sensor network can detect and characterize small urban emission plumes. Outside of this particular case study, it is important to ask questions such as what is the smallest plume that can be detected by a network like $BEACO_2N$, and similarly what is the smallest emission event that can be quantified? For the first question, we can assert that a plume is detectable by the network if the site nearest to the plume sees a robust species concentration enhancement, which we define as an enhancement larger than three times the noise for the instrument in the minute-level measurements. Within the domain of the $BEACO_2N$ network in the San Francisco Bay Area, any arbitrary location is on average 2.5 km away from the nearest measurement site. With an average wind speed of 2.7 m/s in this region, the typical transport time between an emission source and a measurement site is about 15 minutes. The dilution rate then determines the extent to which concentrations are diluted over that transport time. Based on the dilution rate calculated in Figure 3.2 for the plume being studied here, the detection limits for a single emission event plume are shown in Table 3.2. Quantification of the emissions requires a more detailed analysis. To estimate emissions as done above, the plume must be

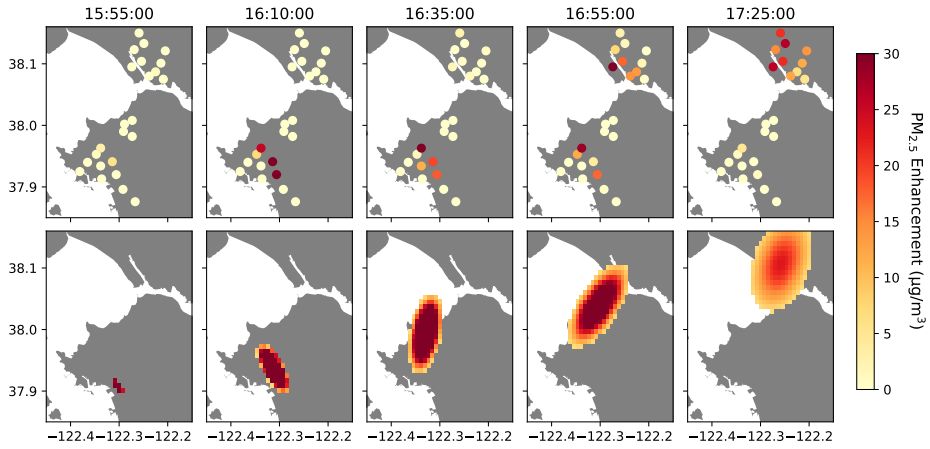

Figure 3.3: $PM_{2.5}$ concentrations at different timepoints during the evolution of the fire plume, from BEACO$_2$N measurements (top row) and the 2-D Gaussian fitting model (bottom row).

measured at multiple sites to properly parameterize the plume. The emission event must be larger to assure that the enhancement remains robust further downwind. Given the 6 parameters in the 2-D Gaussian plume model, we could assert that 6 sites need to measure the plume for it to be quantifiable, and the 6$^{\text{th}}$ closest site is on average 6.5 km away. As such, we define the limit of quantification as the minimum emission needed to produce an enhancement 6.5 km downwind that is larger than three times the noise of the instrument, resulting in the quantification limits shown in Table 3.2. In practice, the measurement time profile at each site allows for a single site to constrain several of the parameters in the Gaussian function, so 6 sites are likely not needed. At the same time, having the plume remain detectable for 6.5 km does not guarantee that it will be measured by 6 sites. Here we assume that these effects more-or-less negate each other to provide a starting threshold for quantification. Importantly, only one species needs to meet this quantification limit for the others to be quantified, given that they are at least detectable. In this case, the quantity of emitted NO_x was too small for the network to parameterize the plume using only NO_x measurements, so the $PM_{2.5}$ concentrations were leveraged to parameterize the plume, and the relative enhancement between NO_x and $PM_{2.5}$ at the first measurement site was used to estimate the NO_x emission quantity. This highlights one of the benefits to a sensor network with an ensemble of species being measured.

Table 3.3 provides context as to the magnitude of typical emissions that one might observe in an urban setting. It is evident that many types of activities will produce detectable plumes in our BEACO$_2$N network, with many of the larger and more continuous sources producing plumes large enough for quantification, prompting a potential direction of future study. It is important to note that several of the sources in Table 3.3 are continuous emission sources.

Table 3.2: Estimates for the $BEACO_2N$ Network's Plume Detection and Quantification Limits

Quantity	CO2 (kg)		CO (kg)		NOx (kg)		PM2.5 (kg)
Limit of Detection	17,000		40		22		8
Limit of Quantification	42,000	or	95	or	53	or	18
Albany Hill Fire	70,000 ± 20,000		2,500 ± 300		28 ± 9		770 ± 30

The values shown for continuous emitters were integrated over 30 minutes, the approximate emission duration for the Albany Hill fire, for comparison. However, continuous and discrete emissions produce different plume profiles and require different parameterizations, so care should be taken in comparing the emissions in Table 3.3 with the reported detection limits.

The variability in plume composition demonstrates the utility in having a multi-pollutant monitoring network. For example, ship emissions are more likely to be noticed in NO_x measurements, whereas a building fire produces significant amounts of PM and CO and relatively little NO_x. With a $BEACO_2N$-like network, both of these types of plumes could be characterized. There are many smaller events that produce plumes below the detection limit listed above. That is not to say that these cannot be detected with a LCS network. Rather, detection needs to happen closer to the source, which can be achieved with a higher network density or strategic placement of the sensors. For example, if sensors were placed such that the closest sensor to any source was on average 500 meters away, the detection limits drop by 35%, allowing for smaller scale plume detection. Advances in the performance of LCSs could enable the measurement of smaller enhancements, further decreasing this limit.

Plume Measurements as a Check on Sensor Network Performance

In a LCS network, it is important to have sensors robustly calibrated before using their data to perform analysis. Conversely, sensors in the field measuring the same plume can provide a check on the robustness of their calibration parameters. In $BEACO_2N$, the $PM_{2.5}$, CO, NO, NO_2 and CO_2 are measured by five separate instruments with five unique calibration schemes.[85–87] Well-calibrated sensors would show consistent pollutant decreases between species over time, assuming these decreases are only from plume dilution. To evaluate our measurements with this assumption, we start by normalizing all the measured enhancements by the enhancement measured at site 25, closest to the fire. This gives us the enhancements as a fraction of the peak enhancement, which we expect to be location-specific and independent of the pollutant measured. Comparing these relative enhancements between $PM_{2.5}$ and CO, we find extremely strong agreement, with a coefficient of determination (R^2) of 0.99. Performing this analysis with CO and CO_2, we find an R^2 of 0.67, which is substantially lower but perhaps unsurprising given the large relative uncertainties for the CO_2 enhancements measured from this event. NO_x was only measurable at one site and thus not amenable to

Table 3.3: Typical GHG and Air Pollutant Emission Quantities from Urban Activities (colored values are above the detection limit from Table 3.2)

Event	CO_2 (kg)	CO (kg)	NO_x (kg)	PM (kg)	Source/Notes
Construction Site †	380	0.22	0.48	0.05	Scaled down from full project emissions assuming 8 hr workday [103]
Car Fire	270	6.9		7.0	Medium-sized automobile, gasoline tank emptied prior to test [104]
Interstate (1 km) †	1700	7.9		0.08	Based on I-580 in Berkeley, CO_2 from [105] and CO and PM from [27]
House Fire	2200	84	3.7	120	Based on 1994 Swedish House Fire Statistics [106]
Cargo Ship †	7500	4.8	260	29	Container ship at 75% load [107]
UCB Powerplant †	7700				Natural gas co-generation plant, scaled down from annual emissions [108]
Waste Incinerator †	19,000	14	36	7.5	EFs from EPA,[109] based on nearest incinerator's annual consumption [110]
Oil Refinery †	230,000				Refinery in Richmond, CA scaled down from annual emissions [111]

† For continuous sources, values are shown for 30 minutes of activity, approximately the duration of the Albany Hill fire

evaluation.

Concluding Remarks and Implications for Sensor Networks

In this work, we quantified emissions from an urban fire using measured pollutant enhancements from its resultant plume as the plume crossed multiple nodes in a densely spaced network. By fitting the enhancements to a 2-D Gaussian plume model, we find the fire to have emitted 770 ± 30 kg of $PM_{2.5}$, 70,000 ± 20,000 kg of CO_2, 2,500 ± 300 kg of CO, and 28 ± 9 kg of NO_x. We use this example to define a plume detection and quantification limit. These limits are the product of both the density of the network (which affects how long a plume travels before reaching a sensor) and the smallest enhancement the sensors can reliably detect (limiting how much plume dilution is allowed over the transport time). While other networks have different measurement densities and sensitivities, this study provides a

general framework for assessing the limits by which sensor networks can contribute towards emissions quantification for both air pollutants and greenhouse gases.

Chapter 4

Using Network Observations to Constrain CO and CO_2 Emissions from an Oil Refinery in the San Francisco Bay Area

This chapter was adapted from: Patel, M. Y.; Asimow, N. G.; Winter, A. R.; Zhu, Y.; Cohen, R. C. Using Network Observations to Constrain CO and CO_2 Emissions from an Oil Refinery in the San Francisco Bay Area. *JGR Atmos.* **2026**, *131*, e2025JD045035.

4.1 Introduction

Cities are major contributors to global greenhouse gas (GHG) emissions, with an estimated 70% of CO_2-eq GHG emissions attributable to urban settlements.[2] Additionally, air pollution is typically more severe in urban areas, with exposure being exacerbated by higher population densities.[112] Efforts to mitigate climate change and improve public health have led to decreases in both GHG and air quality (AQ) emissions, often in specific sectors, leading to a changing emissions map within cities. For example, increasing fuel efficiency and the adoption of electric vehicles has reduced on-road emissions and decreased demand for refined fuel in California, resulting in the planned closure of oil refineries.[82, 113, 114] Many state and local governments have plans for achieving net zero emissions within the next few decades. For example, the state of California has initiated a plan to achieve "carbon neutrality" by 2045 by cutting greenhouse gas emissions 85% below 1990 levels and deploying carbon removal and capture technologies.[115] Governments often rely on activity-based emission inventories to monitor emission changes, but these methods often have large uncertainties.[116, 117] Additionally, many point source emitters monitor emissions through internal monitoring systems, though recent changes in policy may no longer require US companies to make this information publicly available.[118] We believe that independent

verification of both of these approaches by methods such as those described here are a useful tool in support of market-based carbon trading, air quality management, GHG reduction policy and community engagement with emissions from industrial sources.

Emissions within cities are a mix of point (e.g. refineries at the large end of the emission scale or individual manufacturers at the small end of the scale), line (e.g. highways), and area (e.g. residential or commercial neighborhoods) sources. Point sources often produce large quantities of GHGs and air pollutants that can have outsized effects on their surrounding communities. For example, in the city of Richmond, CA, point sources are estimated to account for roughly two-thirds of particulate emissions and over 85% of GHG emissions.[119, 120] These emissions are highly concentrated, producing relatively narrow and variable spatial distributions. The resulting plumes rarely pass near a sparse regulatory network and are often not noticeable in one-hour averages, limiting the effectiveness of ambient regulatory monitoring in assessing pollutant emissions and exposure.

Many approaches including space-based, aircraft, mobile, and sparse fixed location observations have been recently been applied to characterize point source GHG emissions.[121–128] Many of these approaches require resource-intensive measurement campaigns or infrastructure that limit the scope or scale at which they can be applied. Dense networks for AQ and GHG monitoring are emerging as a tool that can be widely deployed at a cost that allows much more detailed and frequent characterization of emissions. These networks have been used to characterize urban emissions using a variety of analytical approaches, often focused on regional or sectoral emissions. For example, Turner et al. evaluated the efficacy of a proposed dense observing network with approximately 2-km spacing.[80] CO_2 network observations have been used to update fine-resolution emissions inventories through the use of inverse modelling.[81–83, 129] However, point source GHG emissions have proven especially difficult to constrain with dense networks in practice as inverse models can alias other emissions (e.g. highways) into the point sources or vice versa.[82] Alternative methods targeted at individual sources have strong potential for constraining point source emissions with dense sensor networks. For example, a simple 2-D Gaussian model was used to quantify the GHG and AQ emissions of a short-lived urban fire observed at multiple locations in the network, leveraging the spatial pattern of measurements to constrain the plume shape and spread.[130] Having independent and robust methods for constraining point source emissions would improve the ability for regional inversion methods to allocate changes in emissions.

Here, we use BEACO$_2$N, an ambient AQ and CO_2 monitoring network, to study and quantify GHG and AQ emissions from an oil refinery in Richmond, CA, a city in the San Francisco Bay Area. We demonstrate the potential for dense ambient monitoring networks to quantify emission rates from continuous point sources by calculating CO_2 emission rates and assess the performance against reported emissions inventories and CO_2 emissions inferred from aircraft observations. Additionally, we measure and assess CO emissions from the refinery, providing novel insight to a potentially large and underestimated source in the city's emissions inventory. Finally, we assess dense networks as a strategy for characterizing point source emissions and make recommendations for approaches to deployment and analysis with broad applicability to the increasingly numerous dense sensor networks around the globe.

4.2 Approach, Site Information, and Methods

Oil Refinery Site Information

The Chevron Richmond Refinery is an oil refinery that has been in operation since 1902.[131] It is the third largest oil refinery in the state of California, refining approximately 250,000 barrels of crude oil per day.[132] The refinery is located in Richmond, CA, a city of roughly 115,000 people and part of the San Francisco Bay Area region of California.[133] West of the refinery site are hills where storage tanks are located and the San Francisco Bay, and east of the site is the city of Richmond, which is mostly below 60 m above sea level. The eastern part of the city rises into the East Bay hills (Figure 4.1). Details about the refinery site and operations can be found in Text C1. From the EPA FLIGHT data (Table C.1) we expect the majority of emissions to come from regions 2 and 3 of the refinery, as defined in Figure 4.1. Region 2 (centered at 37.9498°N, 122.3989°W) is home to the hydroprocessing and fluid catalytic cracking units (FCCUs) for the refining process, and is reported as emitting 792,918 metric tons of CO_2 in 2023.[111] Region 3 (centered at 37.9454°N, 122.3936°W) is where the hydrogen production plant is located, which was reported to have emitted 1,225,083 metric tons of CO_2 in 2023.[111] Hydrogen is used in several refining processes, though less than half of oil refineries produce their own hydrogen on-site.[134] A key assumption in this analysis is that the refinery operations and emissions are continuous over time. Generally, oil refineries operate continuously without pause, though the percent capacity at which they operate may fluctuate for a variety of reasons, including equipment maintenance and malfunctions.[135–137] Oil refineries in the US typically operate with >90% utilization rate.[138, 139] As such, fluctuations in emissions from standard operations are likely minimal.

$BEACO_2N$ Observations

Atmospheric measurements used in this analysis are from the Berkeley Environmental Air-quality and CO_2 Network ($BEACO_2N$), which has been described extensively elsewhere.[24, 84] Briefly, $BEACO_2N$ is deployed in several cities around the globe, with 56 sites currently in operation in the San Francisco Bay Area of California. Each sensor package measures a suite of gases and particles. Most instruments are installed on building rooftops (typically 3-10 m above ground level) at approximately 2 km spacing (see Figure 4.1). CO_2 is measured at 5 s intervals using a Vaisala CARBOCAP Carbon Dioxide Probe GMP343. The CO_2 sensor calibration is described in detail in Delaria et al.[85] Briefly, the sensors have a temperature-dependent offset which is corrected for using comparisons to a reference-grade instrument. Hourly-averaged absolute CO_2 measurements are found to have errors of less than 1.6 ppm. The limit of detection for the instrument, calculated as three times the standard deviation of the noise in the minute-level data, is 2.5 ppm.[130] This is in agreement with the manufacturer's reported ±1 ppm repeatability/noise for 30 s averages.[142] CO, NO, NO_2, and O_3 are measured at 8 s intervals using the Alphasense CO-B4, NO-B4, NO2-B43F, and Ox-B431 electrochemical gas sensors. Calibration methods for these individual

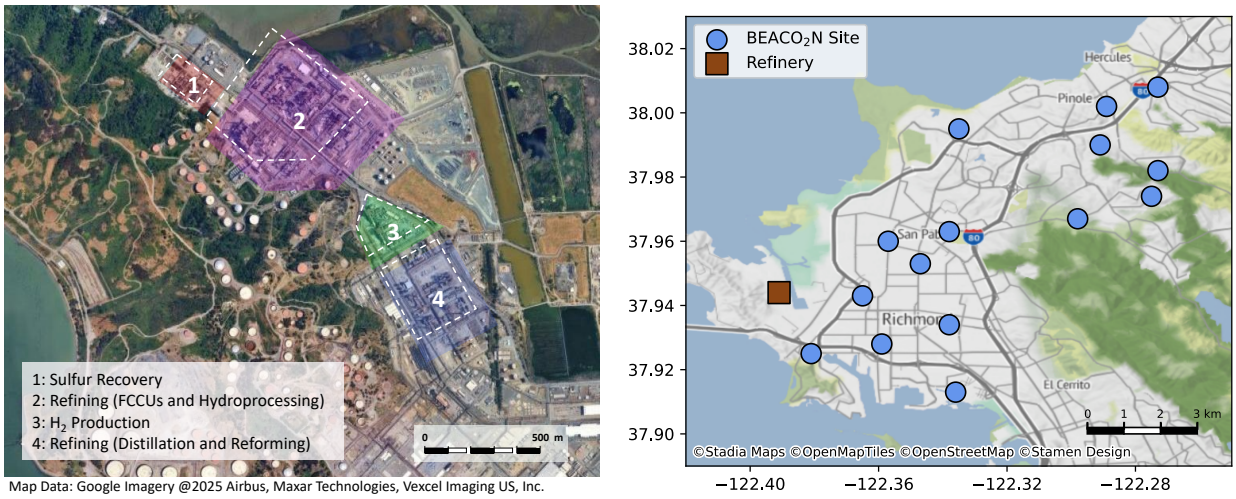

Figure 4.1: Map of (left) Chevron Richmond Refinery with sectoral breakdown,[140, 141] and (right) BEACO$_2$N sites near the refinery used in this study. Background map credits: © Stadia Maps (stadiamaps.com), © Stamen Design (stamen.com), © OpenMapTiles (openmaptiles.org), © OpenStreetMap (openstreetmap.org/copyright).

sensors are presented in Winter et al.[86] The calibrations account for cross-sensitivities and the influences of temperature and humidity at the sensor, as well as drifts in sensitivities and offsets over time. The CO sensor, of main use in this work, was found to not have cross-sensitivities to the other atmospheric gases measured in the BEACO$_2$N node. The CO sensor has a temperature and humidity-dependent offset, which is corrected for with internal temperature and humidity measurements made by an Adafruit BME280 sensor.[47] The calibrated hourly-averaged CO measurements have an uncertainty of 0.033 ppm. The limit of detection (three times the standard deviation of the noise in the minute-level data) is 0.009 ppm.[130] This is slightly higher than the manufacturer's reported noise of 0.006 ppm (3σ).[143] $PM_{2.5}$ is measured at 8 s intervals using a Plantower PMS5003 sensor. $PM_{2.5}$ in the BEACO$_2$N network is calibrated using the methods outlined in Patel et al.[87]

Data were averaged at 1-minute intervals for this study, with all raw data being included without any filtering. CO_2 and CO were analyzed in detail. Measurable enhancements in NO_x and $PM_{2.5}$ coincident with CO_2 plumes were not observed, despite being known pollutants emitted from refineries.[119] Enhancements are likely to be present in the observed plumes but below the detection limits of our sensors: 2 μg m^{-3} for $PM_{2.5}$ and 3.2 ppb for NO_x (M. Y. Patel et al., 2025). Based on these detection limits and the CO_2 emissions reported in this paper, we can only establish an upper limit for NO_x and $PM_{2.5}$ emissions from these two point sources. The upper limit is much larger than the expected NO_x emissions from the refinery of ∼500 tons/yr.[119] Additionally, $PM_{2.5}$ is expected to be emitted from a different mix of processes at the refinery,[119] so its emissions and resultant enhancements are not

expected to be correlated with CO_2 plumes.

Meteorological Parameters

Meteorological inputs were used to both search for plumes and in calculating the emission rate. Meteorological data was taken from the National Oceanic and Atmospheric Administration's (NOAA) High-Resolution Rapid Refresh (HRRR) version 4 model.[144] The model outputs are at 3 x 3 km spatial resolution and hourly temporal resolution. The model parameters used are wind speed and direction (derived from u- and v-wind outputs), low cloud cover, and planetary boundary layer height (PBLH). As an assessment of the model, we compared the NOAA HRRR wind speed and direction to measurements made at a nearby site, Richmond Field Station (37.9131°N, 122.3359°W), measured with a Vaisala WXT520 weather transmitter. The root-mean-square error in wind speed for hourly averaged winds in 2022 was 1.84 m s^{-1}. Deviations were mostly symmetric, with a mean bias of modeled winds found to be $\sim$0.27 m s^{-1} faster than observations. The root-mean-square error in wind direction was 82°, though wind direction is not used in the calculation of the emission rate, so this large uncertainty only impacts the number of plumes detected, as discussed below. The impacts of meteorological variable uncertainties in the analysis are discussed in the section "Plume Model Sensitivity to Parameters" below.

Plume Identification

Point source plumes are narrow and are typically observed as peaks as winds rotate, bringing the plume across the location of a sensor. In favorable conditions, plumes are observed sequentially as winds continue to rotate, bringing the plume to a nearby site or bringing the plume across two sites located along a single trajectory downwind of the source. We focus on the 15 sites shown in Figure 4.1. These are close to the refinery and have high data completeness in the study period of 2022-2023. The prevailing winds are typically from the southwest and blow the refinery plumes over the San Pablo Bay, away from the nearest population centers and our network. We begin by selecting hours when the wind direction is in the range 215-335°, when the wind is broadly blowing from the refinery towards the $BEACO_2N$ sites. This filter greatly reduces the search window for times of potential plume observation. We then searched the data for times with high CO_2 and manually filtered these to identify moments when there were clear and identifiable enhancements. Despite winds typically blowing emissions over the water, the continuous monitoring record provided ample data for this analysis. In total, 266 plume observations across the 15 sites in the years 2022-2023 were identified. This corresponds to roughly 15% of the times filtered by wind. This fraction reflects the broad search window used and cannot be interpreted as the percent of time with favorable winds where we observed a plume.

Given the known uncertainties in modeled wind direction, the wind filter alone does not solely justify attribution of the observed plumes to the refinery. Other evidence includes the magnitude of the CO_2 enhancements which are 10s of ppm, far in excess of other plausible

sources, and that we can trace the trajectories backward from large and coincident enhancements across multiple sites downwind of the refinery (Figure C.4). The latter rules out the possibility of a hyperlocal source near an individual site. There are no other industrial sites in the vicinity of the refinery which the plumes could be attributed to. While there are major highways running through Richmond, they do not produce such concentrated CO_2 plumes as evidenced by other near highway observations in the BEACO$_2$N network. From previous analysis we have found a 1-km stretch of I-580, the nearby highway, to emit $\sim$1% the amount of CO_2 that the refinery is expected to emit.[130] There are no sources in the area that could produce the plumes being studied here other than the refinery. The plumes identified here only simultaneously enhance concentrations for sites in line with the refinery, and enhancements at other sites occur with temporal shifts consistent with a rotating wind field moving the plume trajectory radially from the refinery site (Figure C.5).

Plumes are identified from the 1-min data as enhancements above a baseline concentration. Plumes persisted at measurement sites anywhere from tens of minutes to several hours. For each CO_2 plume observation, the CO_2 and corresponding CO enhancement was calculated (Figure 4.2). The baseline was determined by fitting concentrations before and after the plume (typically 1-2 hours on either end) to a third-degree polynomial. A window of time is then selected as the peak of the plume, at least 10 minutes in length to account for turbulent fluctuations and ensure the measurements are compatible with the plume model parameterizations (discussed below). The enhancement is defined as the difference between the concentrations at the peak and the interpolated baseline at those same times. The uncertainty in the enhancement is defined as the uncertainty in the baseline (the root-mean-square deviation in the baseline fit to the concentrations outside of the plume times) and the uncertainty in the plume height (the standard deviation of the concentrations in the plume peak window) combined in quadrature. For example, the enhancements derived for Figure 4.2 are 49 $\pm$ 4 ppm CO_2 and 0.084 $\pm$ 0.018 ppm CO for the Feb 5, 2023 plume and 42 $\pm$ 2 ppm CO_2 and 0.127 $\pm$ 0.007 ppm CO for the Nov 7, 2023 plume. Strong correlation between the CO and CO_2 concentrations during plume periods indicates that the CO is most likely from a shared source as the CO_2. In Figure 4.2, the Pearson correlations between the two species are 0.86 and 0.94 during the Feb 5, 2023 and Nov 7, 2023 plume periods. Across all observed plumes, the average correlation was 0.81, with 89% of plumes having correlations greater than 0.70.

The Gaussian Plume Model

The Gaussian plume is a simple model used for estimating the 3-D concentration field of a species resulting from a point source emission. The Gaussian plume model is one of many methods for determining emissions from measured concentrations, but offers many benefits, including being applicable to sparse sampling of the concentration field. When comparing different fence-line methods for emissions quantification, Mbua et al. found that the Gaussian plume model showed little bias compared to other methods, and as such produced robust estimations when the measurement sample size was sufficiently large.[126] The model assumes

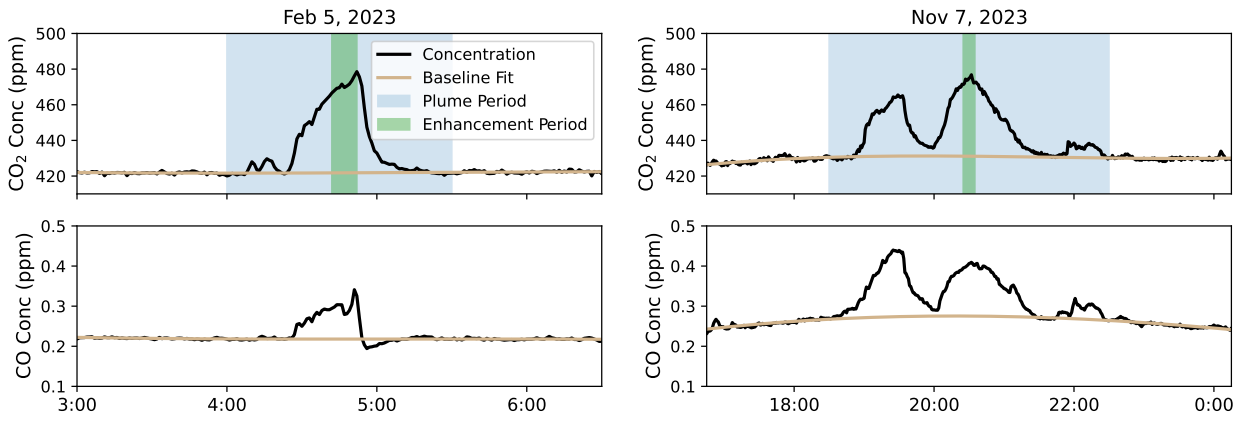

Figure 4.2: Example calculations of the CO_2 and CO enhancements of different observed refinery plumes. The enhancement is calculated as the difference in the concentration and the baseline during the peak enhancement window.

that the wind field is uniform and that the wind field and emission rate are constant over time, producing a time-independent model for concentrations. The model dictates that at a given distance downwind from the source, the concentrations are normally distributed about the center of the plume in both the vertical and horizontal directions. The model can be expressed as:

$$C(x,y,z) = \frac{Q}{U} * \frac{1}{2\pi\sigma_y\sigma_z} e^{-\frac{y^2}{2\sigma_y^2}} \left[e^{-\frac{(z-H)^2}{2\sigma_z^2}} + e^{-\frac{(z+H)^2}{2\sigma_z^2}} + e^{-\frac{(z+H-2L)^2}{2\sigma_z^2}} + e^{-\frac{(z-H-2L)^2}{2\sigma_z^2}} + e^{-\frac{(z-H+2L)^2}{2\sigma_z^2}} \right]$$

where C(x,y,z) is the concentration of the species at a point in space resulting from a point source at location (0,0,H) with an emission rate of Q. In this form, z is the vertical distance, x is the distance along the wind axis, and y is the cross-wind direction in the horizontal plane. From this model, a plume concentration can be defined at each point in space (x,y,z) for a given emission rate and meteorological conditions. The equation can be inverted, and a known concentration from a fixed point in space can be used to determine the emission rate. The $BEACO_2N$ measurements provide the concentration at a fixed point in space, which can be linked to the emission rate through the above equation. As the plume's trajectory changes with wind direction, the measurement sites will sample different parts of the plume over time. The plume concentration should be highest at the centerline, so for each plume observation at a site, the peak enhancement is measured and used in the above equation while setting y=0. When the y=0 assumption is incorrect, estimates of the emission rate will be biased low, though this is negligible if the measurement is within 100 m of the plume centerline (Figure C.3). The wind speed, U, was obtained from NOAA's HRRR model, as detailed above. The parameters σ_y and σ_z are the atmospheric turbulence intensities in the y and z directions, respectively. The turbulence intensities dictate the degree to which the plume spreads away

from the plume centerline both vertically (σ_z) and horizontally (σ_y). Turbulence intensities are parameterized by the Pasquill stability class as a function of downwind distance, x, according to NOAA's Atmospheric Turbulence and Diffusion Laboratory's Handbook on Atmospheric Diffusion.[100] The intensities are parameterized under the assumption that inputs to the model like wind speed and measured concentrations are averaged for at least 10 minutes to fulfill the assumption of a time-averaged plume distribution. The turbulence intensity parameterization used is specific to urban areas to account for the effects of building structures on surface roughness. The Pasquill stability class for each measured plume time is determined based on wind speed, cloud cover, and insolation at each time, with variables obtained from the HRRR model.[145] H is the height of the emission source, adjusted for plume rise. An emission height of 20 m was estimated using satellite imagery of refinery stacks (details found in Text C2). The Gaussian plume model used here contains multiple "reflections" of the plume at the ground (z=0) and at the boundary layer (z=L). These are added to account for the vertical containment of the plume within the planetary boundary layer (PBL). In the equation above, up to two reflections of each plume edge are represented, and adding additional reflections had negligible effects on the results. The PBL height was obtained from the HRRR model and was typically in the range of 200-1000 m.

Plume Model Sensitivity to Input Parameters

In addition to atmospheric composition measurements, the Gaussian plume model requires several inputs to constrain the meteorological conditions of the plume spread during any particular observation. We consider the impacts of these variables in the analysis by performing a series of sensitivity tests, where input parameters are intentionally biased to determine the impact on the final ensemble mean emission rate. Given the ensemble approach taken here, symmetric random errors in any particular parameter will likely have little impact on the average emission rate across all observations, and so systematic biases in the inputs are the most likely source of errors. The outputs of these sensitivity tests are shown in Figure C.3.

The emission height (H) was set to 20 m, and the calculated emission rate is insensitive to the choice of emission height across a wide range of values (Figure C.3). This is due to sufficient vertical mixing of the plume during transport. For example, at 3 km downwind distance and under stability class "E", σ_z is 204 m, so the plume has spread sufficiently to enable sampling near the surface. As such, biases related to calculation of the stack heights and incorporation of plume rise do not impact the final assessment.

NOAA HRRR wind speeds were found to have a bias of +0.27 m s^{-1} compared to nearby ground-based measurements, as discussed above. We find that biasing the wind speed input in the model by the same amount leads to about an 8% increase in the calculated mean emission rate. This is slightly less than the uncertainty range introduced from the measurements themselves as shown in the analysis below. The wind speed is also used to determine the stability class and subsequently the turbulence intensities. Sensitivity to changes in the turbulence intensities are shown in Figure C.3. The effect of wind speed errors on turbulence

intensity are non-linear. For example, when wind speeds are increased 0.27 m s^{-1}, only 5% of the plume observation times see a change in the determined stability class.

PBLH was also taken from NOAA's HRRR model. While PBLH measurements were not readily available for comparison to the model, we explore the sensitivity of the analysis to biases in the modeled PBLH in Figure C.3. Specifically, if we bias the HRRR calculations of PBLH by 20%, the resulting mean emission rate changes <10%. The effects are more severe if HRRR is significantly and systematically overestimating the PBLH. For example, if HRRR PBLH is reduced by 40%, the resulting mean emission rate decreases roughly 20%. We assume there to be no large systematic bias in the HRRR modeled PBL height over the region of interest.

Carbon Mapper Observations

Carbon Mapper is a nonprofit organization aimed at using remote sensing measurements to quantify methane and CO_2 emissions from point sources around the globe. Carbon Mapper has made several aircraft measurements of CO_2 plumes from the refinery in the period from 2018-2022, which are detailed in Table C.3 and used as a point of comparison and discussion in this analysis.[146] Measurements were taken on three separate days during aerial surveys of the San Francisco Bay Area using NASA's Airborne Visible/Infrared Imaging Spectrometer-Next Gen (AVIRIS-NG) instrument. These flights were part of a series of flights aimed at mapping methane sources in the Bay Area and in California more broadly.[147]

4.3 Results and Discussion

CO_2 Emissions Quantification

Here, 266 plume observations made by the BEACO_2N network were analyzed using a Gaussian plume model to estimate the CO_2 emissions from the Chevron Richmond refinery. These plume observations span a two-year period (2022-2023), so in aggregating these observations, we arrive at a time-averaged emission rate for the refinery processes. As detailed in the site information above, most refineries operate continuously and near full operating capacity at all times, so any variations in refinery operations (and subsequent emissions) are minimal and infrequent. To estimate the emission rate Q for each plume observation, the Gaussian plume equation above can be used as described in the methods, where the concentration at a point in space is the measured CO_2 enhancement at a BEACO_2N site. Using these measurements and the necessary meteorological variables from NOAA's HRRR model, the emission rate can be estimated for each observation, producing a distribution of emission rates. However, this assumes that the refinery emissions are a single point source, which is valid at sufficiently far distances, but breaks down for measurements close to the refinery. The refinery is more accurately represented as two major point sources, one for the fluid catalytic cracking units (FCCUs) and hydroprocessing (HP) part of the site, and another for

the H_2 production plant at the site. Within each region, emissions from individual stacks are happening in close enough proximity (Figure C.2) that they coalesce into a single plume from the perspective of a measurement outside the facility. However, as displayed in Figure 4.1, these two regions are approximately 700 m apart from each other, which is significant on the scale of our closest measurement site (∼3 km away). Per the EPA's Facility Level Information on GreenHouse gases Tool (FLIGHT), these two operations emitted roughly 793,000 and 1,225,000 metric tons (mt) CO_2 in 2023, respectively (Table C.1).[111] Assuming uniform emissions across time gives emission rates of roughly 25 kg s^{-1} and 39 kg s^{-1} for the two sectors (Table 4.1). The only other significant emission sector reported on FLIGHT for this refinery was stationary combustion (Table C.1). Our measurements show no indication of these emissions manifesting as large point source plumes, as discussed further below.

In order to make use of all the observations as constraints on the emissions from these two sources, we model a pair of identical emitters evolving downwind according to the Gaussian plume equation (Figure 4.3). The plumes are modeled under the conditions of Pasquill stability class "E", which accounted for roughly 40% of plume observations and was an intermediate meteorological scenario across the stabilities for observations in this work. For the first ∼3 km the two model plumes remain distinct, consistent with the observations of separately identifiable plumes at the site 3 km from the source (detailed below). Further downwind as the plumes merge, the peak CO_2 reaches about 80% of the full value as the resultant plume remains slightly wider than a single source plume would have been, even downwind 12 km. We estimate total emissions from the sum of the two plumes by scaling calculations by the model results shown in Figure 4.3. The resulting emission rates are shown in Figure 4.4, with each point representing the mean rate at BEACO$_2$N site. Importantly, there is no systematic variation in the calculated emission rate with measurement distance from the refinery. The mean emission rate is found to be 61.3 ± 6.3 kg CO_2 s^{-1}, in close agreement to the reports in the EPA FLIGHT database (Table 4.1). Carbon Mapper instantaneous emission rate estimates (Table C.3) from their plume measurements of these two sources are similar.

Table 4.1: CO_2 Plume Emissions (in kg s^{-1}) from the Chevron Richmond Refinery, as Reported in the EPA's FLIGHT Inventory [111] and as Measured by Carbon Mapper [146] and BEACO$_2$N (this work).

	EPA FLIGHT (2023)	**Carbon Mapper (2020–2022)**	**BEACO$_2$N (2022–2023)**
Refining (FCCUs & HP)	25.1	28.1 ± 5.7	35.6 ± 5.6
H_2 Production	38.8	31.0 ± 3.4	25.7 ± 5.0
Total	**63.9**	$\mathbf{59.1 \pm 6.6}$	$\mathbf{61.3 \pm 6.3}$

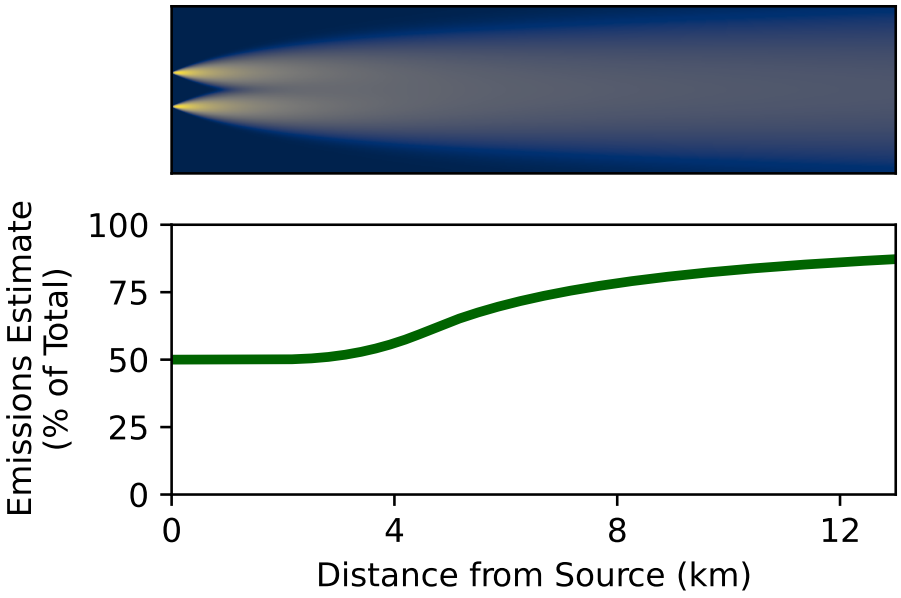

Figure 4.3: (Top) simulated concentration field from two point sources with equivalent emission rates, colored on a log scale. (Bottom) calculated emission rate as a function of the distance from the two point sources, using the Gaussian plume equation, which assumes a single point source (the maximum concentration at each distance is taken as the concentration input for the calculation).

CO Emissions and Process-Level Insights

The BEACO$_2$N network makes simultaneous measurements of CO_2 and air pollutants, providing an observational constraint on emitted pollutants from the refinery. Specifically, the BEACO$_2$N measurements show significant CO enhancements coincident and correlated to CO_2 enhancements observed from the refinery plumes (Figure 4.2). No measurable increase in $PM_{2.5}$ or NO_x was observed in these plumes. Using the enhancements for plume observations where both CO and CO_2 measurements were available, the CO/CO_2 enhancement ratio was calculated. The distribution has a mostly uniform spread of values between 0 and 5 ppb/ppm, with a mean of 2.4 $\pm$ 0.3 ppb/ppm. However, as noted before, the CO_2 plume being observed is likely a confluence of emissions from the two point sources: the FCCU and hydroprocessing region and the hydrogen production plant. For sites measuring in the near field of the refinery, the two source plumes are not well mixed, and plumes of clearly differing composition are observed. An example is shown in Figure 4.5, where the CO/CO_2 enhancement ratio is $\sim$5.0 ppb/ppm in the plume measured from 20:00 – 0:00 local time (LT), whereas the plume measured from 0:00 – 6:00 LT has an enhancement ratio of $\sim$0.6 ppb/ppm. The latter value is consistent with expected FCCU and hydroprocessing emis-

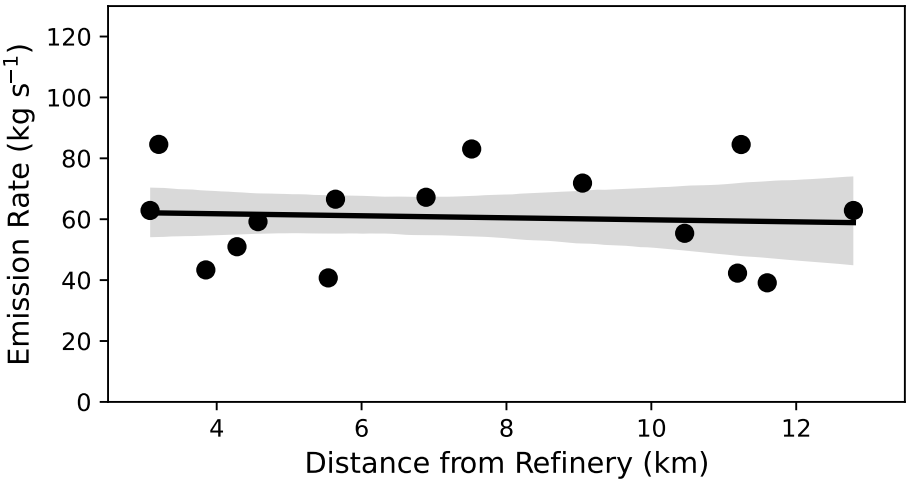

Figure 4.4: Refinery plume mean emission rate calculated at each BEACO$_2$N site, accounting for two point sources, versus distance from the measurement site to the refinery. The line of best fit (black) has no significant slope.

sion ratios, which have been reported to range from 0.28–0.76 ppb/ppm.[148] The Chevron Richmond Refinery uses steam methane reforming (SMR) to produce H_2 by first converting methane and water to CO, and subsequently CO and water to CO_2, with H_2 released at each step.[149] While no literature was found showing the expected CO/CO_2 emission ratio in hydrogen production flue gas, it is possible that such a process would have significant CO emissions given its role as a reaction intermediate. The EPA, in its Emission Estimation Protocol for Petroleum Refineries, says that no default emission factors are available for hydrogen plant vent gases, allowing pollutant emissions to be estimated from a number of methods including efficiency metrics.[150] SMR can have conversion efficiencies from 30% up to 99%,[151] though the excess CH_4/CO/CO_2 mixture can be combined with other fuels to provide combustion heat for the process, further modulating the CO fraction.[152, 153] A conversion efficiency of 99.5% would yield CO/CO_2 emission factors of ∼5 ppb/ppm as observed here.

The distinct plume compositions shown in Figure 4.5 can be used to disaggregate the CO_2 emissions from the two point sources. The two plume periods show ratios of 0.59 ± 0.10 ppb/ppm and 4.98 ± 0.03 ppb/ppm. If we assign the lower ratio to the FCCU/hydroprocessing region of the plant and the higher ratio to the hydrogen production plant as suggested above, the total CO_2 emissions can be separated into the two sectors, since the aggregate CO/CO_2 ratio (2.4 ± 0.3 ppb/ppm) is the sum of the two region-specific ratios weighted by their relative contributions. Doing so, we estimate that 58 ± 7 % of the CO_2 comes from the FCCU and hydroprocessing region, while 42 ± 7% comes from the hydrogen production plant. This CO-based partitioning of the CO_2 between the two point sources is similar to

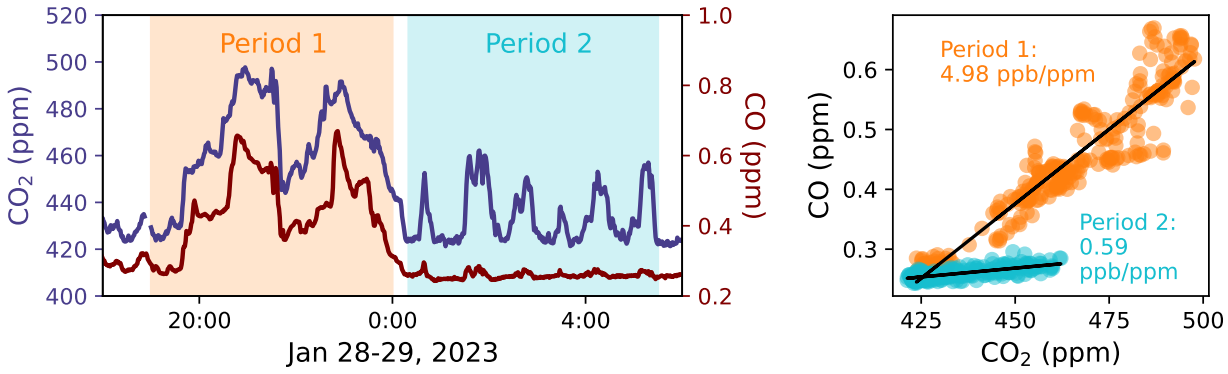

Figure 4.5: CO and CO_2 timeseries at a site near the refinery measuring two plume periods with different compositions on the left, and the corresponding CO/CO_2 enhancement ratios on the right.

the EPA FLIGHT and Carbon Mapper attributions but attributes slightly more CO_2 to the FCCU and hydroprocessing region.

Using the observed CO/CO_2 ratio and the calculated emission rate of 61.3 ± 6.3 kg/s CO_2, it is estimated that the two point sources at the refinery emit an average of 0.094 ± 0.015 kg CO s^{-1}, which amounts to roughly 3000 mt CO per year. Despite the very low emissions as a fraction of the CO_2 (∼0.24%), the point source refinery CO emissions are a substantial fraction of the city's total estimated CO emissions. A 2024 emissions inventory for the Richmond-San Pablo Air Monitoring Community estimates that in the region, 6,800 mt CO were emitted in non-refinery sectors in 2019, while refinery emissions were estimated to be roughly 190 mt,[119] a value 15 times lower than our observations imply.

Insights for Network-Based Point Source Characterization

Here, we constrain CO_2 and CO emission rates from a large point source emitter using multiple downwind plume observations enabled by a densely spaced sensor network. The large enhancements observed (Figure 4.2) imply that these methods could similarly detect and quantify emission rates from point sources with much smaller emission rates than the refinery. Specifically, the average CO_2 enhancement observed at the closest site was ∼37 ppm. Given that, an emission source about 15 times smaller than the refinery (∼4 kg s^{-1}) would be quantifiable if the resultant plumes are distinct from other local sources and influences. This sets the nearest sensor to observe an enhancement of at least 2.5 ppm, which is 3 times the short term noise of the instrument.[130]

The success of this method as implemented here was reliant on a large sample size. Using 266 plume measurements across the 15 sites produced a distribution of emissions estimates. The large spread of this distribution is in part attributed to the errors in using modeled

reanalysis meteorological variables to parameterize the plume. These errors are expected to be symmetric, however, so while individual inferences of emissions from the measurements are noisy, the mean of the distribution is quite robust, as has been found in other implementations of the Gaussian plume model.[126] Measurements of wind and turbulence at each site would provide better constraints on the model and should allow for use of this model with a smaller sample of measurements.

The discussion above focuses on CO_2 but is generally applicable to other species. A multi-pollutant observing network is particularly beneficial in plume analysis, since plumes of differing compositions will enhance different pollutants to varying degrees. For example, fires produce large enhancements in PM, while ships emit large amounts of NO_x.[130] These pollutant species can better trace out certain plumes due to lower ambient concentrations and larger relative sensor sensitivity in the atmosphere compared to CO_2. Overall, GHG and AQ monitoring networks are expected to provide useful constraints on a wide variety of urban plumes.

Several factors can affect the number and frequency of plume detections by a stationary monitoring network. In this work, typical wind patterns advected refinery plumes over the water and greatly limited the number of detections. Additionally, the plumes can be narrow and pass between sparsely placed measurement sites. While these spatial gaps are not a major concern for continuous emissions, they impose restrictions on the observation of episodic events, which are often a concern for communities. For example, flaring events are shown to emit large amounts of air pollutants which can lead to negative health consequences for exposed communities, yet these events are often unplanned and difficult to monitor.[154–156] In such situations, a denser network would limit the likelihood of missed pollutant plumes regardless of meteorological conditions and can be used to provide real-time monitoring of these unplanned episodes.

This method targets large point source plumes and is not the optimal approach for quantifying the stationary combustion emissions from the refinery. Those emissions are reported to account for ∼50% of total CO_2 emissions from the refinery (Table C.1). The spatial distribution of stationary combustion emissions across the refinery site is presumably broad, best represented by many smaller-magnitude sources distributed across the refinery site which cannot be individually assessed with these methods. Emissions that are more distributed are better quantified with other methods, such as the inverse modeling used to calculate total Bay Area CO_2 emissions in our other research.[82, 157]

While the inverse model used in those papers is a widely used method and yields new insights into emissions, we observe that point source plumes are especially challenging to the framework. The sharp concentration gradients caused by large point source emitters, particularly in the near field of the source, can make it challenging to properly apportion enhancements in space at the resolution of typical inverse models (∼1-4km). One of the challenges is related to the resolution of the inversion grid. Based on the typical atmospheric conditions observed in this study, the width of a point source plume would only reach 1 km (σ_y of 500 m) after travelling approximately 10 km downwind. In a 1-km inversion model, observations made close to the site will then greatly over- or under-estimate the true

pixel-wide average concentration since the plume is not yet well mixed to the grid scale. A similar issue arises with the temporal resolution of the model, where a 1-hour timestep may misrepresent the changes in wind direction that can cause sharp changes in measured enhancements within a 1-hour time window. Separate methods for constraining individual point sources may help provide greater stability to regional high-resolution atmospheric inversions.

4.4 Conclusions

Plumes from an oil refinery in Richmond, CA were measured and quantified using a dense sensor network, $BEACO_2N$, with 266 plume observations made over a two-year period. The Gaussian plume model was used to infer emissions from these observations. Modelling the refinery emissions as two point sources, the total emission rate from the two sources was found to be 61.3 $\pm$ 6.3 kg CO_2 s^{-1}, agreeing with self-reported emissions in the EPA FLIGHT inventory and with independent Carbon Mapper measurements. Additionally, the plume measurements had an average CO/CO_2 enhancement ratio of 2.4 $\pm$ 0.3 ppb/ppm, which suggests that the refinery emits roughly 3000 mt CO annually, a substantial portion of the region's total CO emissions.

Chapter 5

Conclusion

As we increasingly try to understand urban emissions with greater specificity and at finer scales, low-cost, dense sensor networks show strong potential to supplement the existing observational systems for atmospheric composition. Dense sensor networks provide high spatial and temporal resolution data for long deployment time periods that can span entire cities and urban domains. Data from these networks can not only help identify emission sources but also disentangle sources in complex emission landscapes, providing information on both source location and emission processes. The BEACO$_2$N network provides such data for many years over the San Francisco Bay Area, measuring both air pollutants and CO_2, providing insights relevant both to climate change and public health goals. In this dissertation, I demonstrate the ability of such a network to provide useful insights into point source emissions within complex urban landscapes.

In Chapter 2, I devised a time-evolving calibration method for the Plantower PMS5003, the PM sensor used in the BEACO$_2$N sensor packages. The calibration uses a hygroscopic growth correction factor derived from κ-Köhler theory to account for particle growth due to ambient humidity. By comparing Plantower readings with EPA AQS reference monitors, I empirically derive the hygroscopic growth factors for $PM_{2.5}$ in the Bay Area and Los Angeles, CA in 2022 and 2023. Importantly, the hygroscopic growth factor shows strong seasonality, with higher values in the summer and lower values in the winter. This matches our expectations based on speciated particle data which shows that particulate sulfate fraction peaks in the summer whereas black carbon fraction peaks in the winter. Allowing the hygroscopic growth factor to change smoothly and sinusoidally over the year reduced seasonal biases in the measurement. Overall, the developed seasonal RH dependence calibration outperformed uncorrected sensor outputs and sensors calibrated with the EPA's national calibration scheme, increasing the utility of $PM_{2.5}$ measurements from the BEACO$_2$N networks in the Bay Area and Los Angeles. Future work should be done to test the generalizability of this method to other regions of the world, given that PM composition follows distinct regional patterns. Additionally, this calibration assumes slow and smooth changes in PM composition over the year and thus is not well suited for unique pollutant events like wildfires, where PM composition and hygroscopicity would be quite different. Such events require

unique corrections to account for the changing aerosol population.

In Chapter 3, I test the ability for a dense sensor network to constrain emissions from a transient pollution event. I used data from the $BEACO_2N$ network to calculate emissions from a small urban fire in Albany, CA in June of 2022. Using measured pollutant enhancements at 1-minute time steps, I used a 2-D Gaussian model to estimate the shape of the pollutant plume produced from the fire and track its path across the region. With this model, I was able to calculate the bulk emissions of $PM_{2.5}$, CO, NO_x, and CO_2 released by the fire. The novel insight brought by the network is highlighted by the fact that this event was not observed by satellite observations nor the EPA AQS network, and transport model simulations incorrectly predicted the trajectory of the fire smoke. Additionally, from this analysis I estimated the limit of detection (observing an event) and the limit of quantification (calculating emission rates) for a $BEACO_2N$-like dense sensor network, which allowed assessment of the utility of these networks in point source quantification. An important conclusion is that a multi-species network greatly increases the scope of events which can be studied, given that different processes have unique emission fingerprints. For example, ships are most likely to be detected through NO_x observations, whereas fires are most apparent in $PM_{2.5}$ or CO enhancements. Overall, I found that limits of detection and quantification are both highly sensitive to the density of the network as well as the sensitivity of the sensors.

In Chapter 4, I used the $BEACO_2N$ network to constrain emissions from a continuous point source emitter, the Richmond Chevron Refinery in Richmond, CA. During a two-year period, 266 plumes were identified across nearby sites as having origins at the refinery. Using the Gaussian plume model, concentration enhancements from $BEACO_2N$ were combined with meteorological data to predict the CO_2 emission rate from the refinery's point sources. The calculated rate, 61.3 ± 6.3 kg s^{-1}, is in close agreement with values from both the EPA's FLIGHT inventory and with independent Carbon Mapper aerial measurements at the site. CO enhancements were also observed, with CO/CO_2 ratios varying between 0–5 ppb/ppm. Additional analysis suggests that the two point sources being identified (the hydrogen production plant and the FCCU/hydroprocessing site) likely have different CO/CO_2 enhancements, with the hydrogen plant likely being an overlooked source of CO emissions from the refinery. The overall calculated CO emissions from the refinery point sources are roughly 15x larger than estimated by the city. The agreement between CO_2 emissions from $BEACO_2N$ calculations and external sources highlights the fidelity of this method, showing that dense sensor networks can be used to constrain point source emissions in cities. Additionally, the CO measurements are a novel external constraint on CO emissions from the refinery and suggest that current inventories may be underestimating their emissions.

These chapters provide only a sampling of case studies for point source detection with the $BEACO_2N$ network, and many other sources remain as future areas for analysis. One promising area of future direction is analysis of ship emissions. The geography of the San Francisco Bay, alongside the presence of a major cargo port and several oil refineries, leads to a large volume of ship traffic with significant consequences for total air pollutant and greenhouse gas emissions. This is particularly pertinent for NO_x emissions, which by some estimates account for $1/5^{th}$ of the regions total NO_x emissions.[158] Shipping emission inventories are reliant

on emission factors that likely do not reflect true conditions, and observational constraints on these emissions are limited and generally reserved for large ships traveling through open waters, where fuel sources and ship engine operations are different from near-coast operations. Networks like BEACO$_2$N have the potential to quantify emissions from individual ships through ambient sampling of shipping plumes. Combined with information from the Automatic Identification System (AIS), observed plumes and emissions can be tied to ship identifications, creating a dataset that links ship type, activity, size, and emissions. This would allow for the construction of a detailed and observationally-constrained shipping emissions inventory, a valuable asset for assessing air pollution effects and monitoring sectoral CO_2 emissions. In a preliminary analysis over a 7 month period at a BEACO$_2$N site on a pier, 110 individual ship NO_x plumes were identified and assigned to specific ships. Plumes were observed from ships across all ship types (cargo, oil tanker, passenger, tug/tow) and simultaneous CO_2 observations allow for the measurement of NO_x/CO_2 enhancement ratios, which appeared to be distinct by ship class. These enhancements can further be used to calculate emission rates with Gaussian plume modeling. Given this, the BEACO$_2$N dataset, combined with plume modeling and AIS ship data, has the potential to construct a Bay Area-specific ship emission inventory with ship class-specific and observationally-constrained emission factors. Methods like these could be further extended to factories, power plants, airports, and other point sources in the BEACO$_2$N domain, providing important constraints to total emission budgets given that large point sources often have outsized contributions to regional emissions.

In this dissertation, I have demonstrated case studies in which dense sensor networks allowed identification and quantification of point source emissions of both air pollutants and CO_2 and extraction of process-level insights, highlighting the many ways in which dense sensor networks can provide additional utility and novel information to our ever-growing atmospheric observing systems. In this network and the many dense networks being deployed worldwide, I believe the datasets generated hold a wealth of information about urban emission sources, and with analytical tools like those presented here, our understanding of urban emissions and the urban atmosphere can be further advanced.

Bibliography

(1) 68% of the world population projected to live in urban areas by 2050, says UN, 2018, https://www.un.org/en/desa/68-world-population-projected-live-urban-areas-2050-says-un.

(2) Dodman, D.; Hayward, B.; Pelling, M.; Broto Castan, V.; Chow, W.; Chu, E.; Dawson, R.; Khirfan, L.; McPhearson, T.; Prakash, A.; Zheng, Y.; Ziervogel, G. In *Climate Change 2022: Impacts, Adaptation and Vulnerability*, Pörtner, H.-O., Roberts, D., Tignor, M., Poloczanska, E., Mintenbeck, K., Alegría, A., Craig, M., Langsdorf, S., Löschke, S., Möller, V., Okem, A., Rama, B., Eds.; Cambridge University Press: Cambridge, UK and New York, NY, USA, 2022, pp 907–1040, DOI: 10.1017/9781009325844.008.

(3) *State of Global Air 2025*; tech. rep.; 2025 Health Effects Institute, 2025, https://www.stateofglobalair.org/resources/report/state-global-air-report-2025.

(4) *Air Quality and Health in Cities: A State of Global Air Report*; tech. rep.; 2022 Health Effects Institute, 2022, https://www.stateofglobalair.org/resources/health-in-cities.

(5) Space agencies play a key role for Global Greenhouse Gas Watch, 2025, https://wmo.int/media/update/space-agencies-play-key-role-global-greenhouse-gas-watch.

(6) TEMPO: A New Era of Air Quality Monitoring from Space, 2020, https://www.epa.gov/sciencematters/tempo-new-era-air-quality-monitoring-space.

(7) Jacob, D. J.; Varon, D. J.; Cusworth, D. H.; Dennison, P. E.; Frankenberg, C.; Gautam, R.; Guanter, L.; Kelley, J.; McKeever, J.; Ott, L. E.; Poulter, B.; Qu, Z.; Thorpe, A. K.; Worden, J. R.; Duren, R. M. *Atmospheric Chemistry and Physics* **2022**, *22*, 9617–9646, DOI: 10.5194/acp-22-9617-2022.

(8) Aerosol Properties & Processes: Projects, https://csl.noaa.gov/groups/csl2/projects.html.

(9) Airborne Missions, https://airbornescience.nasa.gov/program/airborne_missions.

(10) Xia, T.; Borjigin, S. G.; Raneses, J.; Stroud, C. A.; Batterman, S. A. *Atmosphere* **2023**, *14*, DOI: 10.3390/atmos14060906.

(11) Wietzel, J. B.; Korben, P.; Hoheisel, A.; Schmidt, M. *Atmospheric Measurement Techniques* **2025**, *18*, 4631–4645, DOI: 10.5194/amt-18-4631-2025.

(12) Albertson, J. D.; Harvey, T.; Foderaro, G.; Zhu, P.; Zhou, X.; Ferrari, S.; Amin, M. S.; Modrak, M.; Brantley, H.; Thoma, E. D. *Environmental Science and Technology* **2016**, *50*, 2487–2497, DOI: 10.1021/acs.est.5b05059.

(13) Ars, S.; Vogel, F.; Arrowsmith, C.; Heerah, S.; Knuckey, E.; Lavoie, J.; Lee, C.; Pak, N. M.; Phillips, J. L.; Wunch, D. *Environmental Science and Technology* **2020**, *54*, 15671–15679, DOI: 10.1021/acs.est.0c05386.

(14) Apte, J. S.; Manchanda, C. *Science* **2024**, *385*, 380–385, DOI: 10.1126/science.adq3678.

(15) Apte, J. S.; Messier, K. P.; Gani, S.; Brauer, M.; Kirchstetter, T. W.; Lunden, M. M.; Marshall, J. D.; Portier, C. J.; Vermeulen, R. C.; Hamburg, S. P. *Environmental Science and Technology* **2017**, *51*, 6999–7008, DOI: 10.1021/acs.est.7b00891.

(16) Aerosol Robotic Network, https://aeronet.gsfc.nasa.gov/.

(17) Atmospheric Science and Chemistry mEasurement NeTwork, https://ascent.research.gatech.edu/.

(18) Total Carbon Column Observing Network, https://www.tccon.caltech.edu/.

(19) Pandora Project, https://pandora.gsfc.nasa.gov/.

(20) Clean Air Status and Trends Network, https://www.epa.gov/castnet.

(21) Interagency Monitoring of Protected Visual Environments.

(22) Air Quality System (AQS), https://www.epa.gov/aqs.

(23) Okorn, K.; Iraci, L. T. *Atmospheric Measurement Techniques* **2024**, *17*, 6425–6457, https://doi.org/10.5194/amt-17-6425-2024.

(24) Shusterman, A. A.; Teige, V. E.; Turner, A. J.; Newman, C.; Kim, J.; Cohen, R. C. *Atmospheric Chemistry and Physics* **2016**, *16*, 13449–13463, DOI: 10.5194/acp-16-13449-2016.

(25) Cohen, A. J. et al. *The Lancet* **2017**, *389*, 1907–1918, DOI: 10.1016/S0140-6736(17)30505-6, http://dx.doi.org/10.1016/S0140-6736(17)30505-6.

(26) Kim, K. H.; Kabir, E.; Kabir, S. *Environment International* **2015**, *74*, 136–143, DOI: 10.1016/j.envint.2014.10.005, http://dx.doi.org/10.1016/j.envint.2014.10.005.

(27) Fitzmaurice, H. L.; Cohen, R. C. *Atmospheric Chemistry and Physics* **2022**, *22*, 15403–15411, DOI: 10.5194/acp-22-15403-2022.

(28) Kuula, J.; Mäkelä, T.; Aurela, M.; Teinilä, K.; Varjonen, S.; González, Ó.; Timonen, H. *Atmospheric Measurement Techniques* **2020**, *13*, 2413–2423, DOI: 10.5194/amt-13-2413-2020.

(29) Molina Rueda, E.; Carter, E.; L'Orange, C.; Quinn, C.; Volckens, J. *Environmental Science and Technology Letters* **2023**, *10*, 247–253, DOI: 10.1021/acs.estlett.3c00030.

(30) Ouimette, J.; Malm, W.; Schichtel, B.; Sheridan, P.; Andrews, E.; Ogren, J.; Arnott, W. P. *Atmospheric Measurement Techniques Discussions* **2022**, *15*, 655–676, DOI: 10.5194/amt-2021-170.

(31) Ambient Monitoring Technology Information Center *List of Designated Reference and Equivalent Methods*; tech. rep.; 2022, www.epa.gov/ttn/amtic/criteria.html).

(32) Giordano, M. R.; Malings, C.; Pandis, S. N.; Presto, A. A.; McNeill, V. F.; Westervelt, D. M.; Beekmann, M.; Subramanian, R. *Journal of Aerosol Science* **2021**, *158*, 105833, DOI: 10.1016/j.jaerosci.2021.105833, https://doi.org/10.1016/j.jaerosci.2021.105833.

(33) Petters, M. D.; Kreidenweis, S. M. *Atmospheric Chemistry and Physics* **2007**, *13*, 1961–1971, DOI: 10.5194/acp-13-1081-2013.

(34) Han, J.; Liu, X.; Chen, D.; Jiang, M. *Journal of Aerosol Science* **2020**, *139*, 105462, DOI: 10.1016/j.jaerosci.2019.105462, https://doi.org/10.1016/j.jaerosci.2019.105462.

(35) Hänel, G. *Tellus A: Dynamic Meteorology and Oceanography* **1968**, *20*, 371–379, DOI: 10.3402/tellusa.v20i3.10016.

(36) Mackey, K. R.; Stragier, S.; Robledo, L.; Cat, L. A.; Xu, X.; Capps, S.; Treseder, K. K.; Czimczik, C. I.; Faiola, C. *Atmospheric Environment* **2021**, *244*, 117795, DOI: 10.1016/j.atmosenv.2020.117795, https://doi.org/10.1016/j.atmosenv.2020.117795.

(37) Sayahi, T.; Butterfield, A.; Kelly, K. E. *Environmental Pollution* **2019**, *245*, 932–940, DOI: 10.1016/j.envpol.2018.11.065.

(38) Stavroulas, I.; Grivas, G.; Michalopoulos, P.; Liakakou, E.; Bougiatioti, A.; Kalkavouras, P.; Fameli, K. M.; Hatzianastassiou, N.; Mihalopoulos, N.; Gerasopoulos, E. *Atmosphere* **2020**, *11*, 926, DOI: 10.3390/atmos11090926.

(39) Hagan, D. H.; Kroll, J. H. *Atmospheric Measurement Techniques* **2020**, *13*, 6343–6355, DOI: 10.5194/amt-13-6343-2020.

(40) Crilley, L. R.; Shaw, M.; Pound, R.; Kramer, L. J.; Price, R.; Young, S.; Lewis, A. C.; Pope, F. D. *Atmospheric Measurement Techniques* **2018**, *11*, 709–720, DOI: 10.5194/amt-11-709-2018.

(41) Di Antonio, A.; Popoola, O. A.; Ouyang, B.; Saffell, J.; Jones, R. L. *Sensors* **2018**, *18*, 2790, DOI: 10.3390/s18092790.

(42) Malings, C.; Tanzer, R.; Hauryliuk, A.; Saha, P. K.; Robinson, A. L.; Presto, A. A.; Subramanian, R. *Aerosol Science and Technology* **2020**, *54*, 160–174, DOI: 10.1080/02786826.2019.1623863, https://doi.org/10.1080/02786826.2019.1623863.

(43) Nilson, B.; Jackson, P. L.; Schiller, C. L.; Parsons, M. T. *Atmospheric Measurement Techniques* **2022**, *15*, 3315–3328, DOI: https://doi.org/10.5194/amt-2021-425.

(44) Barkjohn, K. K.; Gantt, B.; Clements, A. L. *Atmospheric Measurement Techniques* **2021**, *14*, 4617–4637, DOI: 10.5194/amt-14-4617-2021.

(45) Kumar, V.; Sahu, M. *Journal of Aerosol Science* **2021**, *157*, 105809, DOI: 10.1016/j.jaerosci.2021.105809, https://doi.org/10.1016/j.jaerosci.2021.105809.

(46) Plantower *Plantower PMS5003 Data Manual*; tech. rep.; 2016, http://www.aqmd.gov/docs/default-source/aq-spec/resources-page/plantower-pms5003-manual_v2-3.pdf.

(47) Adafruit Industries *Adafruit BME280 Humidity + Barometric Pressure + Temperature Sensor Breakout*; tech. rep.; 2023, pp 1–34, https://learn.adafruit.com/adafruit-bme280-humidity-barometric-pressure-temperature-sensor-breakout/overview.

(48) Cerully, K. M.; Bougiatioti, A.; Hite, J. R.; Guo, H.; Xu, L.; Ng, N. L.; Weber, R.; Nenes, A. *Atmospheric Chemistry and Physics* **2015**, *15*, 8679–8694, DOI: 10.5194/acp-15-8679-2015.

(49) Chen, Y.; Wang, Y.; Nenes, A.; Wild, O.; Song, S.; Hu, D.; Liu, D.; He, J.; Hildebrandt Ruiz, L.; Apte, J. S.; Gunthe, S. S.; Liu, P. *Environmental Science and Technology* **2022**, *56*, 7163–7173, DOI: 10.1021/acs.est.2c00650.

(50) Virtanen, P. et al. *Nature Methods* **2020**, *17*, 261–272, DOI: 10.1038/s41592-019-0686-2.

(51) Wu, Z. J.; Zheng, J.; Shang, D. J.; Du, Z. F.; Wu, Y. S.; Zeng, L. M.; Wiedensohler, A.; Hu, M. *Atmospheric Chemistry and Physics* **2016**, *16*, 1123–1138, DOI: 10.5194/acp-16-1123-2016.

(52) Kaur, K.; Kelly, K. E. *Atmospheric Measurement Techniques Discussions* **2022**, *16*, 2455–2470, DOI: https://doi.org/10.5194/amt-16-2455-2023, https://amt.copernicus.org/preprints/amt-2022-292/.

(53) Holder, A. L.; Mebust, A. K.; Maghran, L. A.; McGown, M. R.; Stewart, K. E.; Vallano, D. M.; Elleman, R. A.; Baker, K. R. *Sensors* **2020**, *20*, 4796, DOI: 10.3390/s20174796.

(54) deSouza, P.; Barkjohn, K.; Clements, A.; Lee, J.; Kahn, R.; Crawford, B.; Kinney, P. *Environmental Science: Atmospheres* **2023**, *3*, 521–536, DOI: 10.1039/d2ea00142j.

(55) Penza, M., *Low-cost sensors for outdoor air quality monitoring*; Elsevier Inc.: 2019, pp 235–288, DOI: 10.1016/B978-0-12-814827-3.00012-8, http://dx.doi.org/10.1016/B978-0-12-814827-3.00012-8.

(56) Carotenuto, F.; Bisignano, A.; Brilli, L.; Gualtieri, G.; Giovannini, L. *Meteorological Applications* **2023**, *30*, e2161, DOI: 10.1002/met.2161.

(57) Caubel, J. J.; Cados, T. E.; Preble, C. V.; Kirchstetter, T. W. *Environmental Science and Technology* **2019**, *53*, 7564–7573, DOI: 10.1021/acs.est.9b00282.

(58) Heimann, I.; Bright, V. B.; McLeod, M. W.; Mead, M. I.; Popoola, O. A.; Stewart, G. B.; Jones, R. L. *Atmospheric Environment* **2015**, *113*, 10–19, DOI: 10.1016/j.atmosenv.2015.04.057, http://dx.doi.org/10.1016/j.atmosenv.2015.04.057.

(59) Frederickson, L. B.; Sidaraviciute, R.; Schmidt, J. A.; Hertel, O.; Johnson, M. S. *Atmospheric Chemistry and Physics* **2022**, *22*, 13949–13965, DOI: 10.5194/acp-22-13949-2022.

(60) Baruah, A.; Zivan, O.; Bigi, A.; Ghermandi, G. *Environmental Science: Atmospheres* **2023**, *3*, 830–841, DOI: 10.1039/d2ea00165a.

(61) Heintzelman, A.; Filippelli, G. M.; Moreno-Madriñan, M. J.; Wilson, J. S.; Wang, L.; Druschel, G. K.; Lulla, V. O. *International Journal of Environmental Research and Public Health* **2023**, *20*, 1934, DOI: 10.3390/ijerph20031934.

(62) Zaidan, M. A.; Xie, Y.; Motlagh, N. H.; Wang, B.; Nie, W.; Nurmi, P.; Tarkoma, S.; Petaja, T.; Ding, A.; Kulmala, M. *IEEE Sensors Journal* **2022**, *22*, 23507–23520, DOI: 10.1109/JSEN.2022.3216071.

(63) Gurram, S.; Stuart, A. L.; Pinjari, A. R. *Computers, Environment and Urban Systems* **2019**, *75*, 22–34, DOI: 10.1016/j.compenvurbsys.2019.01.002, https://doi.org/10.1016/j.compenvurbsys.2019.01.002.

(64) Parvez, F.; Wagstrom, K. *Air Quality, Atmosphere and Health* **2020**, *13*, 271–279, DOI: 10.1007/s11869-019-00786-6.

(65) Santiago, J. L.; Rivas, E.; Gamarra, A. R.; Vivanco, M. G.; Buccolieri, R.; Martilli, A.; Lechón, Y.; Martín, F. *Science of the Total Environment* **2022**, *819*, 152062, DOI: 10.1016/j.scitotenv.2021.152062.

(66) Wilson, J. G.; Kingham, S.; Pearce, J.; Sturman, A. P. *Atmospheric Environment* **2005**, *39*, 6444–6462, DOI: 10.1016/j.atmosenv.2005.07.030.

(67) Considine, E. M.; Braun, D.; Kamareddine, L.; Nethery, R. C.; Desouza, P. *Environmental Science and Technology* **2022**, *53*, 1391–1402, DOI: 10.1021/acs.est.2c06626.

(68) Shah, A. S.; Lee, K. K.; McAllister, D. A.; Hunter, A.; Nair, H.; Whiteley, W.; Langrish, J. P.; Newby, D. E.; Mills, N. L. *BMJ* **2015**, *350*, h1295, DOI: 10.1136/BMJ.h1295.

(69) Cosselman, K. E.; Allen, J.; Jansen, K. L.; Stapleton, P.; Trenga, C. A.; Larson, T. V.; Kaufman, J. D. *Environmental Research* **2020**, *191*, 110027, DOI: 10.1016/j.envres.2020.110027, https://doi.org/10.1016/j.envres.2020.110027.

(70) Urch, B.; Silverman, F.; Corey, P.; Brook, J. R.; Lukic, K. Z.; Rajagopalan, S.; Brook, R. D. *Environmental Health Perspectives* **2005**, *113*, 1052–1055, DOI: 10.1289/ehp.7785.

(71) Link, M. S.; Luttmann-Gibson, H.; Schwartz, J.; Mittleman, M. A.; Wessler, B.; Gold, D. R.; Dockery, D. W.; Laden, F. *Journal of the American College of Cardiology* **2013**, *62*, 816–825, DOI: 10.1016/j.jacc.2013.05.043.

(72) Di, Q.; Dai, L.; Wang, Y.; Zanobetti, A.; Choirat, C.; Schwartz, J. D.; Dominici, F. *Journal of the American Medical Association* **2017**, *318*, 2446–2456, DOI: 10.1001/jama.2017.17923.

(73) Blundell, W.; Kokoza, A. *Journal of Public Economics* **2022**, *208*, 104601, DOI: 10.1016/j.jpubeco.2022.104601, https://doi.org/10.1016/j.jpubeco.2022.104601.

(74) Cushing, L. J.; Chau, K.; Franklin, M.; Johnston, J. E. *Environmental Research Letters* **2021**, *16*, 034032, DOI: 10.1088/1748-9326/abd3d4.

(75) Kanabkaew, T.; Mekbungwan, P.; Raksakietisak, S.; Kanchanasut, K. *Environmental Pollution* **2019**, *252*, 543–552, DOI: 10.1016/j.envpol.2019.05.082, https://doi.org/10.1016/j.envpol.2019.05.082.

(76) Crawford, B.; Hagan, D. H.; Grossman, I.; Cole, E.; Holland, L.; Heald, C. L.; Kroll, J. H. *Proceedings of the National Academy of Sciences of the United States of America* **2021**, *118*, 1–7, DOI: 10.1073/pnas.2025540118.

(77) Subramanian, R.; Ellis, A.; Torres-Delgado, E.; Tanzer, R.; Malings, C.; Rivera, F.; Morales, M.; Baumgardner, D.; Presto, A.; Mayol-Bracero, O. L. *ACS Earth and Space Chemistry* **2018**, *2*, 1179–1186, DOI: 10.1021/acsearthspacechem.8b00079.

(78) Nguyen, P. D.; Martinussen, N.; Mallach, G.; Ebrahimi, G.; Jones, K.; Zimmerman, N.; Henderson, S. B. *International Journal of Environmental Research and Public Health* **2021**, *18*, 9811, DOI: 10.3390/ijerph18189811.

(79) Liu, G.; Moore, K.; Su, W. C.; Delclos, G. L.; Gimeno Ruiz de Porras, D.; Yu, B.; Tian, H.; Luo, B.; Lin, S.; Lewis, G. T.; Craft, E.; Zhang, K. *Science of the Total Environment* **2022**, *849*, 157881, DOI: 10.1016/j.scitotenv.2022.157881, https://doi.org/10.1016/j.scitotenv.2022.157881.

(80) Turner, A. J.; Shusterman, A. A.; McDonald, B. C.; Teige, V.; Harley, R. A.; Cohen, R. C. *Atmospheric Chemistry and Physics* **2016**, *16*, 13465–13475, DOI: 10.5194/acp-16-13465-2016.

(81) Turner, A. J.; Kim, J.; Fitzmaurice, H.; Newman, C.; Worthington, K.; Chan, K.; Wooldridge, P. J.; Köehler, P.; Frankenberg, C.; Cohen, R. C. *Geophysical Research Letters* **2020**, *47*, 1–6, DOI: 10.1029/2020GL090037.

(82) Asimow, N. G.; Turner, A. J.; Cohen, R. C. *Environmental Science and Technology* **2024**, *58*, 6586–6594, DOI: 10.1021/acs.est.3c09642.

(83) Lian, J. et al. *Atmospheric Chemistry and Physics* **2023**, *23*, 8823–8835, DOI: 10.5194/acp-23-8823-2023.

(84) Shusterman, A. A.; Kim, J.; Lieschke, K. J.; Newman, C.; Wooldridge, P. J.; Cohen, R. C. *Atmospheric Chemistry and Physics* **2018**, *18*, 13773–13785, DOI: 10.5194/acp-18-13773-2018.

(85) Delaria, E. R.; Kim, J.; Fitzmaurice, H. L.; Newman, C.; Wooldridge, P. J.; Worthington, K.; Cohen, R. C. *Atmospheric Measurement Techniques* **2021**, *14*, 5487–5500, DOI: 10.5194/amt-14-5487-2021.

(86) Winter, A. R.; Zhu, Y.; Asimow, N. G.; Patel, M. Y.; Cohen, R. C. *Environmental Science & Technology* **2025**, *59*, 2599–2610.

(87) Patel, M. Y.; Vannucci, P. F.; Kim, J.; Berelson, W. M.; Cohen, R. C. *Atmospheric Measurement Techniques* **2024**, *17*, 1051–1060.

(88) Delp, W. W.; Singer, B. C. *Sensor* **2020**, *20*, 3683.

(89) Liang, Y.; Sengupta, D.; Campmier, M. J.; Lunderberg, D. M.; Apte, J. S.; Goldstein, A. H. *Proceedings of the National Academy of Sciences of the United States of America* **2021**, *118*, 1–6, DOI: 10.1073/pnas.2106478118.

(90) A Statement from the City of Albany on the Fires in the Albany Hill Area on June 26, 2022, 2022, https://www.albanyca.org/Home/Components/News/News/11999/15.

(91) Bartlett, A. Evacuations in Albany are lifted after grass fire breaks out, 2022, https://www.sfgate.com/california-wildfires/article/Evacuations-ordered-for-Bay-Area-residents-as-17267152.php.

(92) Flores, J. Woman Arrested for Allegedly Setting Albany Hill Fire that Prompted Evacuations, 2022, https://www.sfchronicle.com/eastbay/article/Woman-arrested-for-allegedly-setting-Albany-Hill-17268757.php.

(93) Li, C.; Cohen, R. C. *Journal of Geophysical Research: Atmospheres* **2021**, *126*, 1–16, DOI: 10.1029/2020JD033883.

(94) Emerson, E. W.; Hodshire, A. L.; DeBolt, H. M.; Bilsback, K. R.; Pierce, J. R.; McMeeking, G. R.; Farmer, D. K. *Proceedings of the National Academy of Sciences of the United States of America* **2020**, *117*, 26076–26082, DOI: 10.1073/pnas.2014761117.

(95) Cape, J. N.; Coyle, M.; Dumitrean, P. *Atmospheric Environment* **2012**, *59*, 256–263, DOI: 10.1016/j.atmosenv.2012.05.030, http://dx.doi.org/10.1016/j.atmosenv.2012.05.030.

(96) Anderson, L. D.; Dix, B.; Schnell, J.; Yokelson, R.; Veefkind, J. P.; Ahmadov, R.; de Gouw, J. *Geophysical Research Letters* **2023**, *50*, e2023GL105811, DOI: 10.1029/2023GL105811.

(97) Urbanski, S. *Forest Ecology and Management* **2014**, *317*, 51–60, DOI: 10.1016/j.foreco.2013.05.045, http://dx.doi.org/10.1016/j.foreco.2013.05.045.

(98) Gkatzelis, G. I. et al. *Atmospheric Chemistry and Physics* **2024**, *24*, 929–956, DOI: 10.5194/acp-24-929-2024.

(99) Urbanski, S. P.; Hao, W. M.; Baker, S. *Developments in Environmental Science* **2008**, *8*, 79–107, DOI: 10.1016/S1474-8177(08)00004-1.

(100) Hanna, S. R.; Briggs, G. A.; Hosker Jr., R. P., *Handbook on Atmospheric Diffusion*; Smith, J. S., Ed.; US Department of Energy Technical Information Center: 1982.

(101) Du, H.; Zeng, F.; Peng, W.; Wang, K.; Zhang, H.; Liu, L.; Song, T. *Forests* **2015**, *6*, 1763–1778, DOI: 10.3390/f6061763.

(102) Keith, H.; Raison, R. J.; Jacobsen, K. L. *Plant and Soil* **1997**, *196*, 81–99, DOI: 10.1023/A:1004286030345.

(103) Sandanayake, M.; Zhang, G.; Setunge, S. *Environmental Impact Assessment Review* **2018**, *68*, 1–9, DOI: 10.1016/j.eiar.2017.09.003, https://doi.org/10.1016/j.eiar.2017.09.003.

(104) Lönnermark, A.; Blomqvist, P. *Chemosphere* **2006**, *62*, 1043–1056, DOI: 10.1016/j.chemosphere.2005.05.002.

(105) Fitzmaurice, H. L.; Turner, A. J.; Kim, J.; Chan, K.; Delaria, E. R.; Newman, C.; Wooldridge, P.; Cohen, R. C. *Atmospheric Chemistry and Physics* **2022**, *22*, 3891–3900, DOI: 10.5194/acp-22-3891-2022.

(106) Persson, B.; Simonson, M. *Fire Technology* **1998**, *34*, 266–279, DOI: 10.1023/a:1015350024118.

(107) Khan, M. Y.; Ranganathan, S.; Agrawal, H.; Welch, W. A.; Laroo, C.; Miller, J. W.; Cocker, D. R. *Journal of the Air and Waste Management Association* **2013**, *63*, 284–291, DOI: 10.1080/10962247.2012.744370.

(108) Lee, J. UC Berkeley's power plant: At the end of its lifetime, Berkeley, CA, 2021, https://www.dailycal.org/weekender/features/uc-berkeley-s-power-plant-at-the-end-of-its-lifetime/article_efa14b27-849f-5688-a5f3-97b31f784333.html.

(109) AP 42, Fifth Edition, Volume I Chapter 2: Solid Waste Disposal, 2024, https://www.epa.gov/air-emissions-factors-and-quantification/ap-42-fifth-edition-volume-i-chapter-2-solid-waste-0.

(110) Carlson, K. Garbage-burning plant in Stanislaus County plagued by financial issues. Will it close?, 2024.

(111) Facility Level Information on GreenHouse gas Tool, https://ghgdata.epa.gov/%0D%0A.

(112) Health Effects Institute Air Quality and Health in Cities: A State of Global Air Report, Boston, MA, 2022.

(113) Merten, P. How California's decreasing gasoline sales compare nationwide, 2024.

(114) Udasin, S. Refinery closures increase uncertainty about California's fuel future, 2025, https://thehill.com/policy/equilibrium-sustainability/5280032-california-fuel-refinery-closures-gas-prices-newsom/.

(115) *2022 Scoping Plan for Achieving Carbon Neutrality*; tech. rep.; Sacramento, CA: California Air Resources Board, 2022, https://ww2.arb.ca.gov/sites/default/files/2022-11/2022-sp.pdf.

(116) Gately, C. K.; Hutyra, L. R. *Journal of Geophysical Research: Atmospheres* **2017**, *122*, 242–11, DOI: 10.1002/2017JD027359.

(117) Gurney, K. R.; Liang, J.; Roest, G.; Song, Y.; Mueller, K.; Lauvaux, T. *Nature Communications* **2021**, *12*, 553, DOI: 10.1038/s41467-020-20871-0, http://dx.doi.org/10.1038/s41467-020-20871-0.

(118) *Proposed Rule: Reconsideration of the Greenhouse Gas Reporting Program*; tech. rep.; US Environmental Protection Agency, 2025, https://www.epa.gov/system/files/documents/2025-09/reconsideration-of-ghgrp-proposal-fact-sheet.pdf.

(119) *Path to Clean Air: Richmond, North Richmond & San Pablo Community Emissions Reduction Plan*; tech. rep.; Richmond, CA: Bay Area Air Quality Management District, 2024, pp 22–60, https://www.baaqmd.gov/~/media/files/ab617-community-health/richmond/2024/042024-final-ptca-plan-files/ptca-plan_final_april-2024-pdf.pdf?rev=275660fc2f6c4eecaa35b13451b99856&sc_lang=en.

(120) *Richmond General Plan 2030 Element 8: Energy and Climate Change*; tech. rep.; Richmond, CA: City of Richmond, 2012, https://www.ci.richmond.ca.us/2608/General-Plan-2030.

(121) Chen, W. et al. *Journal of Geophysical Research: Atmospheres* **2024**, *129*, DOI: 10.1029/2023JD040284.

(122) Cusworth, D. H.; Duren, R. M.; Thorpe, A. K.; Eastwood, M. L.; Green, R. O.; Dennison, P. E.; Frankenberg, C.; Heckler, J. W.; Asner, G. P.; Miller, C. E. *AGU Advances* **2021**, *2*, e2020AV000350, DOI: 10.1029/2020av000350.

(123) Eapi, G. R.; Sabnis, M. S.; Sattler, M. L. *Journal of the Air and Waste Management Association* **2014**, *64*, 927–944, DOI: 10.1080/10962247.2014.907098, http://dx.doi.org/10.1080/10962247.2014.907098.

(124) Hugenholtz, C. H.; Vollrath, C.; Gough, T.; Wearmouth, C.; Fox, T.; Barchyn, T.; Billinghurst, C. *Journal of the Air and Waste Management Association* **2021**, *71*, 1319–1332, DOI: 10.1080/10962247.2021.1942316, https://doi.org/10.1080/10962247.2021.1942316.

(125) Kim, J.; Berelson, W. M.; Rollins, N. E.; Asimow, N. G.; Newman, C.; Cohen, R. C.; Miller, J. B.; McDonald, B. C.; Peischl, J.; Lehman, S. J. *Environmental Science and Technology* **2025**, *59*, 3508–3517, DOI: 10.1021/acs.est.4c11392.

(126) Mbua, M.; Riddick, S. N.; Kiplimo, E.; Zimmerle, D. *EGUsphere [preprint]* **2024**, *preprint*, https://doi.org/10.5194/egusphere-2024-3161.

(127) Nassar, R.; Hill, T. G.; McLinden, C. A.; Wunch, D.; Jones, D. B.; Crisp, D. *Geophysical Research Letters* **2017**, *44*, 045–10, DOI: 10.1002/2017GL074702.

(128) Zhang, Z.; Cusworth, D. H.; Ayasse, A. K.; Sherwin, E. D.; Brandt, A. R. *Geophysical Research Letters* **2023**, *50*, e2023GL105755, DOI: 10.1029/2023GL105755.

(129) Turnbull, J. C. et al. *Environmental Science and Technology* **2019**, *53*, 287–295, DOI: 10.1021/acs.est.8b05552.

(130) Patel, M. Y.; Zhu, Y.; Winter, A. R.; Asimow, N. G.; Cohen, R. C. *ACS ES&T Air* **2025**, *2*, 1099–1106, DOI: 10.1021/acsestair.5c00069.

(131) About Chevron in Richmond, https://richmond.chevron.com/about.

(132) California's Oil Refineries, 2024, https://www.energy.ca.gov/data-reports/energy-almanac/californias-petroleum-market/californias-oil-refineries.

(133) Community Profile, https://www.ci.richmond.ca.us/241/Community-Profile.

(134) *Available and Emerging Technologies for Reducing Greenhouse Gas Emissions from the Petroleum Refining Industry*; tech. rep.; Research Triangle Park, NC: U.S. Environmental Protection Agency, 2010, https://19january2021snapshot.epa.gov/sites/static/files/2015-12/documents/refineries.pdf.

(135) *ABB Oil and Gas*, https://new.abb.com/oil-and-gas/sectors/refining-and-petrochemicals.

(136) *Nature* **2024**, *629*, 259, DOI: 10.1038/d41586-024-01323-x.

(137) *Global Electronic Services*.

(138) Hack, K.; Harris, J. *U. S Energy Information Administration* **2024**, https://www.eia.gov/todayinenergy/detail.php?id=62624.

(139) *American Fuel & Petrochemical Manufacturers* **2022**, https://www.afpm.org/newsroom/blog/refinery-utilization-101-other-half-capacity-story.

(140) Gosney, D. Welcome to the Chevron Refinery, Richmond, CA, 2019, https://www.radiofreerichmond.com/welcome_to_the_chevron_refinery.

(141) Lindsay, B.; Riddle, R. Chevron Richmond Refinery Revised Renewal Project Conditional Use Permit / Amended EIR Application, 2011, https://www.ci.richmond.ca.us/DocumentView.aspx?DID=7207.

(142) Vaisala *GMP343 Carbon Dioxide Probe*; tech. rep.; Vaisala, 2020, https://docs.vaisala.com/v/u/B210688EN-H/en-US.

(143) Alphasense *CO-B4/CO-B4+ Carbon Monoxide Sensor*; tech. rep.; Alphasense, https://ametekcdn.azureedge.net/mediafiles/project/oneweb/oneweb/alphasense/products/datasheets/alphasense_co-b4_datasheet_en_2.pdf?revision:87f7d42e-02c4-4b00-b888-bd9c8d07ed3f.

(144) NOAA The High Resolution Rapid Refresh HRRRv3 [Dataset], 2025, https://rapidrefresh.noaa.gov/hrrr.

(145) Pasquill Stability Classes, https://www.ready.noaa.gov/READYpgclass.php.

(146) Carbon Mapper, data.carbonmapper.org.

(147) AVIRIS-NG Flight Logs.

(148) Sun, P.; Young, B.; Elgowainy, A.; Lu, Z.; Wang, M.; Morelli, B.; Hawkins, T. *Environmental Science and Technology* **2019**, *53*, 6556–6569, DOI: 10.1021/acs.est.8b05870, https://doi.org/10.1021/acs.est.8b05870.

(149) Hydrogen Production: Natural Gas Reforming, https://www.energy.gov/eere/fuelcells/hydrogen-production-natural-gas-reforming.

(150) Coburn, J.; Schaffner, K.; Sroka, K.; Cunningham, J.; Randall, D.; Richardson Fry, C.; Icenhour, M. Emission Estimation Protocol for Petroleum Refineries Version 2.1.1, 2011.

(151) Ganguli, A.; Bhatt, V. *Frontiers in Thermal Engineering* **2023**, *3*, 1–15, DOI: 10.3389/fther.2023.1143987.

(152) Chevron Products Company Richmond Refinery: Greenhouse Gas Emission Reductions from Hydrogen Plant Replacement at the Richmond Refinery, 2021, https://ww2.arb.ca.gov/sites/default/files/2021-03/2021-0319-chevron-report.pdf.

(153) Process Solutions Guide: Refining - Hydrogen Plant, https://www.emerson.com/documents/automation/training-refining-process-solution-guide-hydrogen-plant-micro-motion-en-65904.pdf.

(154) Osuji, L. C.; Avwiri, G. O. *Chemistry and Biodiversity* **2005**, *2*, 1277–1289, DOI: 10.1002/cbdv.200590099.

(155) Ozymy, J.; Jarrell, M. L. *Review of Policy Research* **2011**, *28*, 365–382, DOI: 10.1111/j.1541-1338.2011.00502.x.

(156) Tran, H.; Polka, E.; Buonocore, J. J.; Roy, A.; Trask, B.; Hull, H.; Arunachalam, S. *GeoHealth* **2024**, *8*, e2023GH000938, DOI: 10.1029/2023GH000938.

(157) Asimow, N. G.; Patel, M. Y.; Zhu, Y.; Winter, A. R.; Gurney, K. R.; Berelson, W. M.; Turner, A.; Cohen, R. C. *Geophysical Research Letters* **2025**, *52*, e2025GL115772, DOI: 10.1029/2025GL115772, https://doi.org/10.1029/2025GL115772.

(158) Guha, A.; Husain, A.; Nguyen, M.; Tang, N.; Claire, S.; Dinh, T.; Lau, V.; Du, Y. *Bay Area Emissions Inventory Summary for Criteria Air Pollutants*; tech. rep. February 2024; Bay Area Air Quality Management District, https://www.baaqmd.gov/en/about-air-quality/emission-inventory.

Appendix A

Supplemental Material for "Towards a hygroscopic growth calibration for low-cost $PM_{2.5}$ sensors"

This chapter was adapted from the supplement of: Patel, M. Y.; Vannucci, P. F.; Kim, J.; Berelson, W. M.; Cohen, R. C. Towards a hygroscopic growth calibration for low-cost $PM_{2.5}$ sensors. *Atmos. Meas. Tech.* **2024**, *17*, 1051-1060.

Table A.1: Summary statistics for the datasets from the Laney and LA sites for Plantower $PM_{2.5}$ measurements (PM $PM_{2.5}$, in µg/m^3), BME relative humidity measurements (RH, %), and EPA AQS $PM_{2.5}$ measurements (AQS $PM_{2.5}$, in µg/m^3).

		Laney			LA	
Statistic	PT $PM_{2.5}$	RH	AQS $PM_{2.5}$	PT $PM_{2.5}$	RH	AQS $PM_{2.5}$
count	17024	17024	17024	12701	12701	12701
mean	9.74	51.83	9.11	12.14	46.89	13.41
std	10.58	18.79	6.34	9.86	22.88	8.39
min	0.00	2.48	-5.0	0	1.22	-3.0
25%	2.71	34.94	5.0	5.14	27.29	8.2
50%	6.13	55.41	8.0	9.67	46.23	12.0
75%	11.97	67.68	12.0	16.15	67.84	17.0
max	73.52	100	60.0	144.51	100	265.3

Table A.2: Sinusoidal fitting parameters for κ, m, and the Sulfate and EC fractions at the Laney Site as shown in Figure 2.1. The sine wave takes the form $y = a * \sin \frac{2\pi}{365}(x - \delta) + b$ where x is the day of the year and the phase shift δ has units of days. The goodness of fit is given by r, the Pearson Correlation between the true values and the sine wave fit.

y	a	b	δ	r
κ (2021)	0.286	0.498	53.3	0.73
κ (2022)	0.242	0.366	72.8	0.86
m (2021)	0.998	1.668	53.2	0.85
m (2022)	0.745	1.429	73.6	0.89
Sulfate Frac	0.046	0.091	94.0	0.63
EC Frac	0.046	0.071	265.8	0.74

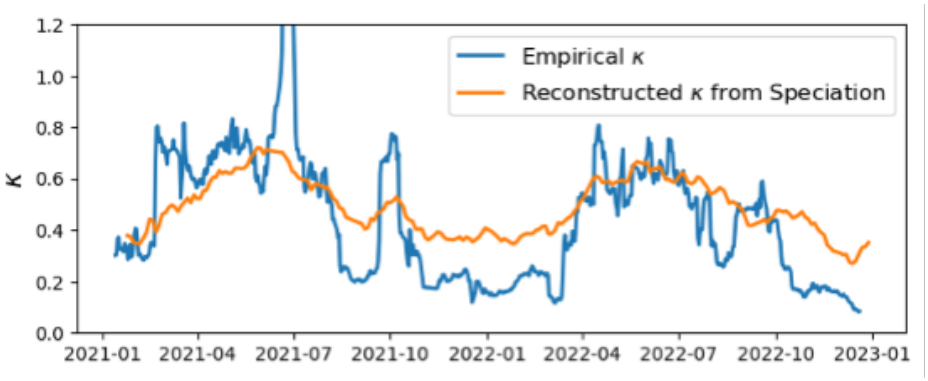

Figure A.1: Empirically calculated κ for the Laney site (Table 1), as shown in Figure 2.1, alongside κ reconstructed from particle speciation data, displayed as a 4-week rolling average. Note the speciation data is not collocated with the $PM_{2.5}$ measurements. An organic matter/organic carbon ratio of 1.6 was used to assign the organic matter fraction of the particle.

Table A.3: Monthly performance statistics for the sensor at Laney, relative to the co-located EPA AQS site, before and after the calibration was applied (r: Pearson Correlation Coefficient, MFB: Mean Fractional Bias, NRMSE: Normalized Root-Mean-Square Error).

	Before			After		
Month	r	MFB	NRMSE	r	MFB	NRMSE
Jan 2021	0.818	0.455	0.918	0.842	-0.021	0.43
Feb 2021	0.740	-0.023	0.666	0.808	-0.101	0.529
Mar 2021	0.711	-0.305	0.558	0.789	-0.152	0.461
Apr 2021	0.666	-0.335	0.486	0.768	-0.087	0.343
May 2021	0.611	-0.406	0.553	0.755	-0.145	0.365
Jun 2021	0.728	-0.433	0.702	0.84	-0.205	0.479
Jul 2021	0.564	-0.154	0.54	0.714	0.035	0.452
Aug 2021	0.825	0.134	0.47	0.863	0.203	0.519
Sep 2021	0.782	0.107	0.606	0.836	-0.021	0.543
Oct 2021	0.727	-0.358	0.581	0.815	-0.575	0.684
Nov 2021	0.862	0.809	1.051	0.914	-0.1	0.263
Dec 2021	0.902	0.971	1.563	0.914	-0.004	0.425
Jan 2022	0.886	0.925	1.157	0.924	0.202	0.363
Feb 2022	0.862	0.446	0.896	0.896	0.187	0.555
Mar 2022	0.622	-0.2	0.57	0.726	-0.272	0.491
Apr 2022	0.647	-0.325	0.549	0.731	-0.201	0.459
May 2022	0.721	-0.406	0.577	0.808	-0.208	0.427
Jun 2022	0.674	-0.345	0.537	0.77	-0.127	0.431
Jul 2022	0.716	-0.263	0.57	0.783	-0.112	0.5
Aug 2022	0.741	-0.109	0.533	0.794	-0.015	0.517
Sep 2022	0.570	-0.201	0.515	0.705	-0.211	0.453
Oct 2022	0.728	0.123	0.556	0.764	-0.164	0.417
Nov 2022	0.870	0.181	0.627	0.901	-0.27	0.412
Dec 2022	0.916	0.391	0.918	0.934	-0.253	0.384

Table A.4: Sinusoidal fitting parameters for κ, m, and the Sulfate and EC fractions at the LA Site as shown in Figure 2.6. The sine wave takes the form $y = a * \sin \frac{2\pi}{365}(x - \delta) + b$ where x is the day of the year and the phase shift δ has units of days. The goodness of fit is given by r, the Pearson Correlation between the true values and the sine wave fit.

y	a	b	δ	r
κ	0.057	0.248	34.9	0.36
m	0.211	1.307	70.0	0.65
Sulfate Frac	0.072	0.115	100.5	0.77
EC Frac	0.042	0.086	267.9	0.64

Table A.5: Performance statistics for the sensor in LA relative to its nearest EPA AQS site with different calibration schemes applied (R^2: Coefficient of Determination, RMSE: Root-Mean-Square Error)

Calibration Scheme	R^2	RMSE ($\mu g/m^3$)
No Calibration	0.312	6.96
National EPA Calibration	0.116	7.89
Seasonal RH Calibration	0.472	6.09

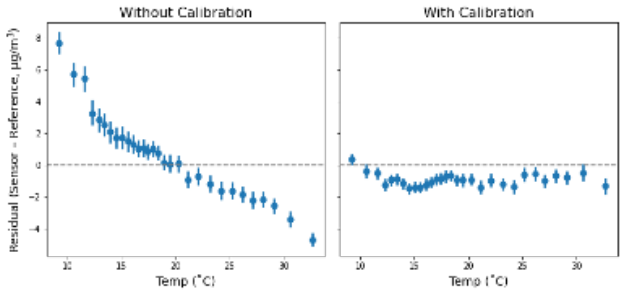

Figure A.2: Measurement residuals (Sensor output – EPA AQS values) for Laney data without and with the seasonal RH dependence calibration, binned into 30 temperature bins.

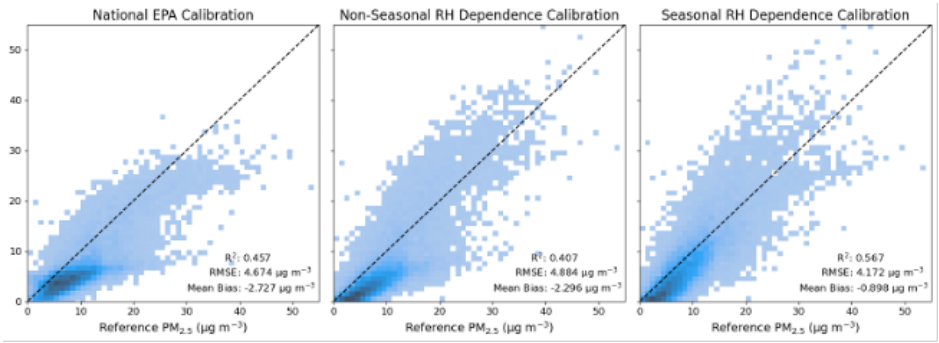

Figure A.3: Sensor predicted $PM_{2.5}$ values versus EPA reference values for Laney site from 2021–2022 with different correction algorithms. The non-seasonal RH dependence calibration uses a constant optimized κ and m value ($\kappa = 0.311$, m = 1.02) rather than values changing sinusoidally in time (Figure 2.1). Performance metrics are the Coefficient of Determination (R^2), root-mean-square error (RMSE), and mean bias.

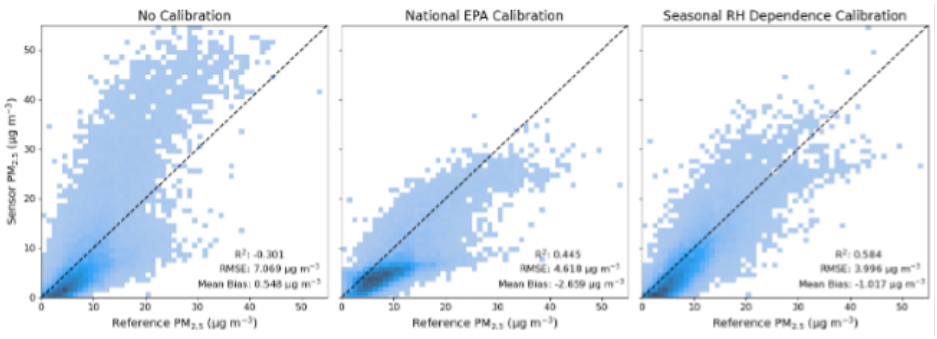

Figure A.4: Reproduction of Figure 2.4 with bad air quality days (Aug 20 – Sep 16, 2021) removed. Sensor predicted $PM_{2.5}$ values versus EPA reference values for Laney site from 2021–2022 with different correction algorithms. Performance metrics are the Coefficient of Determination (R^2), root-mean-square error (RMSE), and mean bias.

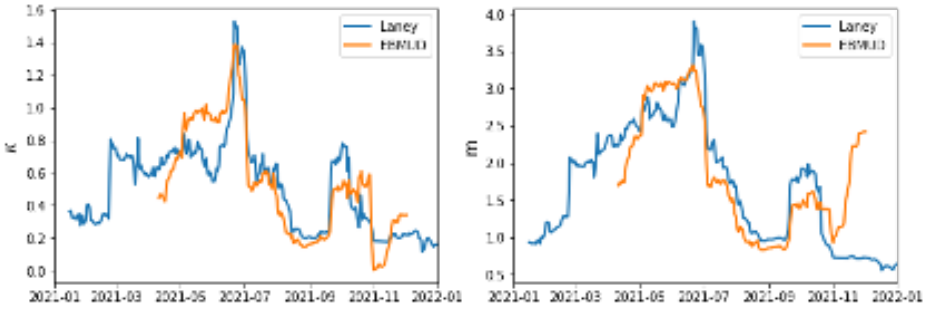

Figure A.5: Calculated calibration parameters for two co-location sites in the Bay Area, CA: Laney and EBMUD (Table 2.1).

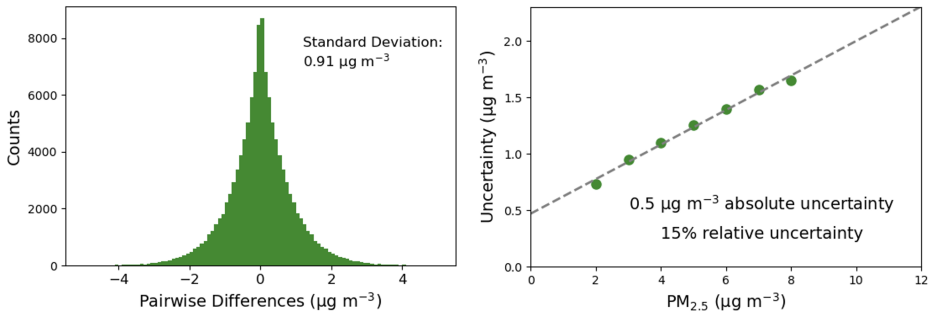

Figure A.6: Pairwise differences of 17 Plantowers from two different manufacturer batches from 2 months of co-location in lab show that instrument noise is about 1 µg m^{-3}, similar to the manufacturer's reported uncertainty. Analysis by size bin shows that the uncertainty is an absolute uncertainty of about 0.5 µg m^{-3} with an added relative uncertainty of about 15%.

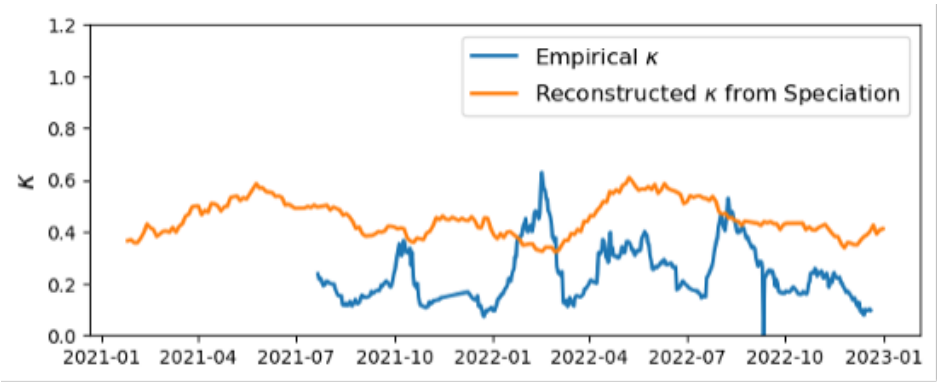

Figure A.7: Empirically calculated κ for the Los Angeles site (Table 2.1), as shown in Figure 2.6, alongside κ reconstructed from particle speciation data, displayed as a 4-week rolling average. An organic matter/organic carbon ratio of 1.6 was used to assign the organic matter fraction of the particle.

Appendix B

Supplemental Material for "Plume Detection and Emissions Quantification Potential Using a Dense Sensor Network"

This chapter was adapted from the supplement of: Patel, M. Y.; Zhu, Y.; Winter, A. R.; Asimow, N. G.; Cohen, R. C. Plume Detection and Emissions Quantification Potential Using a Dense Sensor Network. *ACS EST Air* **2025**, *2*, 1099-1106.

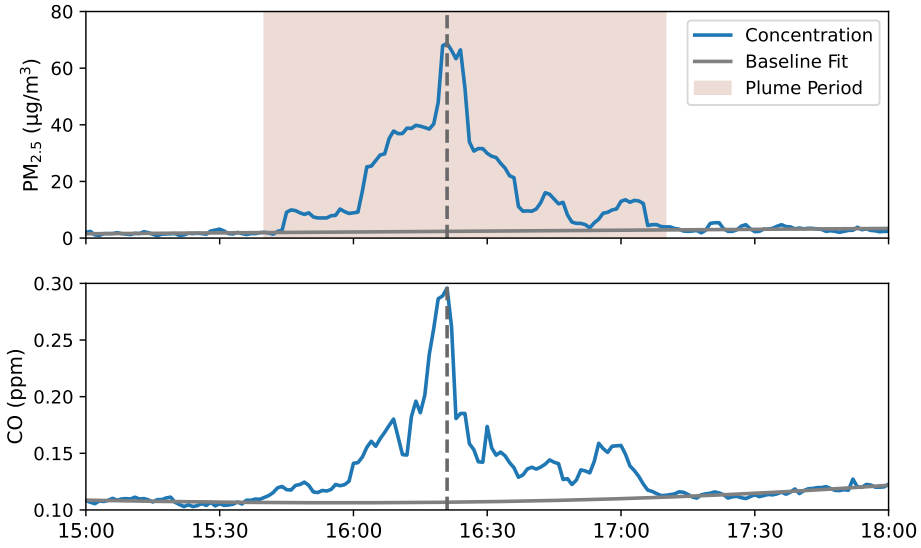

Figure B.1: $PM_{2.5}$ and CO enhancements at site 23 shown in blue, with the baseline fit shown as the grey line, fitted to data outside the shaded region. Enhancements are calculated at the time indicated by the grey dashed line.

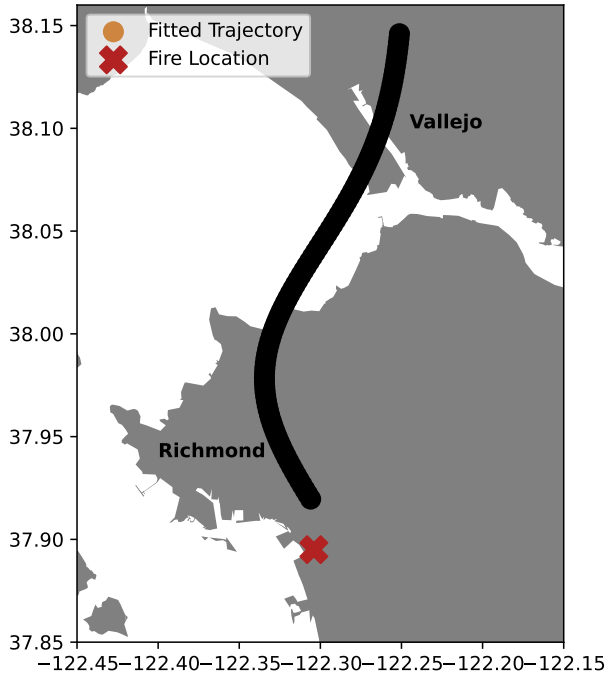

Figure B.2: Fire location and the trajectory from the plume (x_0 and y_0 from the Gaussian equation) from the Gaussian fitting of the concentrations.

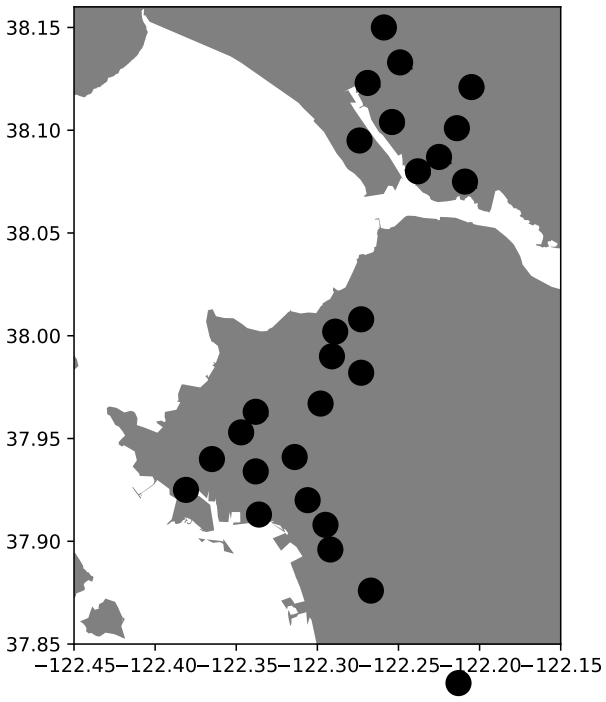

Figure B.3: $BEACO_2N$ sites in the region of interest. Sites with site ID labeled observed the smoke plume.

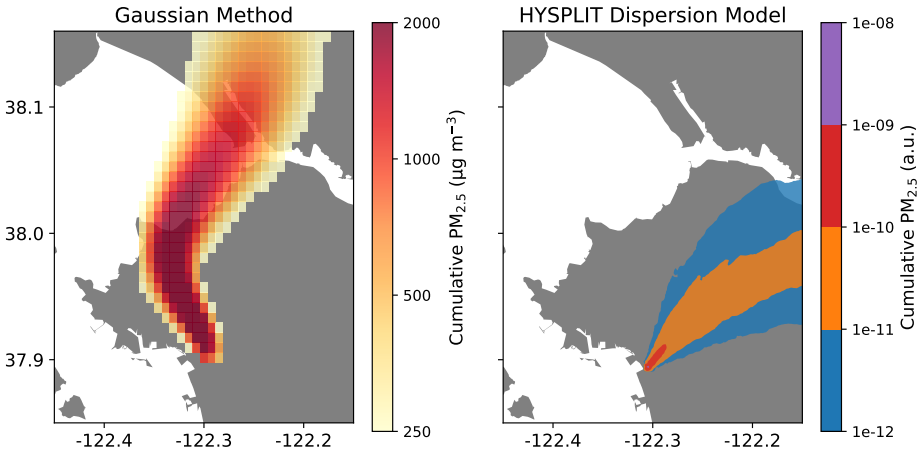

Figure B.4: Cumulative $PM_{2.5}$ concentrations for the fitted Gaussian model (left) and from NOAA HYSPLIT Dispersion model (right).

Appendix C

Supplemental Material for "Using Network Observations to Constrain CO and CO_2 Emissions from an Oil Refinery in the San Francisco Bay Area"

This chapter was adapted from the supplement of: Patel, M. Y.; Asimow, N. G.; Winter, A. R.; Zhu, Y.; Cohen, R. C. Using Network Observations to Constrain CO and CO_2 Emissions from an Oil Refinery in the San Francisco Bay Area. *JGR Atmos.* **2026**, *131*, e2025JD045035.

Text C1. Chevron Richmond Refinery Site and Operations

While the oil refining process is interconnected, the Chevron Richmond refinery site contains several process-specific sections as shown in Figure C.1 below.[140, 141] Region 1 is where the sulfur recovery occurs. Gases with high hydrogen sulfide concentrations are treated to reduce the emissions of hydrogen sulfide compounds into the atmosphere. Region 2 is where the hydroprocessing and fluid catalytic cracking units (FCCUs) are located. FCCUs use heat, pressure, and catalysts to convert heavy hydrocarbon molecules into lighter ones. Hydroprocessing includes the use of hydrogen gas to facilitate this process. Region 3 is the hydrogen production plant, where steam-methane reforming (SMR) is used to convert methane to hydrogen gas. Hydrogen gas is used for hydroprocessing and desulfurization. Region 4 is where distillation and reforming occurs. Distillation is the process of separating fuel components into different products based on their boiling points. Reforming is a process using heat and pressure to convert naphtha, one of the distillation fractions, into a gasoline component.

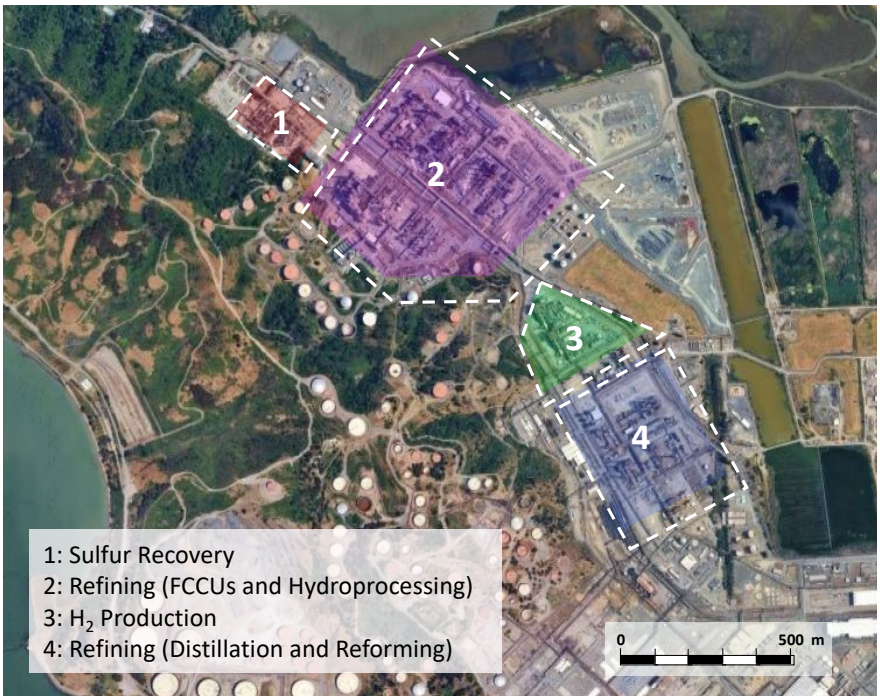

Figure C.1: Map of the Chevron Richmond Refinery, with regions corresponding to sectors in Table C.1

The US EPA requires large facilities to report emissions of greenhouse gases. This data is found in the EPA's Facility Level Information on GreenHouse gases Tool (FLIGHT).[111] The information is provided with sectoral breakdown, as shown in Table C.1. The largest emission source is from stationary fuel combustion; however, it is not clear where this process happens and if it is distributed or concentrated. The other two large CO_2 emission sectors, fluid catalytic cracking units (FCCUs) and hydrogen production, can both be spatially located and produce large identifiable plumes. The marked locations of these emission sources are in agreement with aerial measurements of CO_2 plumes found by Carbon Mapper (Table C.3).

Text C2. Plume Height Estimation

To determine the height of the emission sources, satellite imagery was used to measure the length and azimuthal angle of the shadows cast by the emission stacks, which can be used to determine the height of the stack. The height of the stack, h, is related to the length of the shadow, d, through the equation:

$$h = d \tan \theta_s$$

Table C.1: Richmond Chevron Refinery Sectors and Reported CO_2 Emissions from the EPA FLIGHT Inventory (mt = metric tons)

Map Identifier	Sector	CO_2 Emissions (2023)
1	Sulfur Recovery	14,980 mt
2	Refining: FCCUs and Hydroprocessing	792,918 mt
3	H_2 Production	1,225,083 mt
4	Refining: Distillation and Reforming	90 mt
–	Stationary Fuel Combustion	2,300,394 mt

where θ_s is the solar zenith angle. The solar zenith angle can be determined from the azimuthal angle of the shadow, ϕ_s, with the equation:

$$\theta_s = \sin^{-1}\left(\frac{\sin\delta}{\sqrt{\cos^2(\phi_s)\cos^2(\Phi) + sin^2(\Phi)}}\right) - \tan^{-1}\left(\frac{\sin\Phi}{\cos\phi_s\cos\Phi}\right)$$

where Φ is the angle of latitude and δ is the declination of the sun, which is a function of the day of the year, N, and can be approximated as:

$$\delta \approx -23.44^\circ * \cos\left(\frac{360^\circ}{365} * (N+10)\right)$$

The stack heights were measured at multiple stacks with visible emissions, which were found to correspond to Carbon Mapper plume origin locations. These locations in regions 2 and 3 of Figure C.1 are shown in Figure S2, with the corresponding calculated heights shown in Table C.2. The average across all 7 measured stacks is about 17.7 m. The two stacks at the hydrogen production plant are taller than the stacks in the refining section. However, as shown in Figure C.3, the analysis is highly insensitive to the choice in emission height, so this difference is unlikely to impact any of the analyses. Additionally, the emission height used in the Gaussian plume model should account for plume rise, though this will depend on several unknown factors, including the vertical velocity and source temperature of the emitted gas. Given the insensitivity of the analysis to the chosen source height (Figure C.3), the true plume rise is not considered further, and we instead use 20 m as an estimated average emission source height.

Additional Tables and Figures

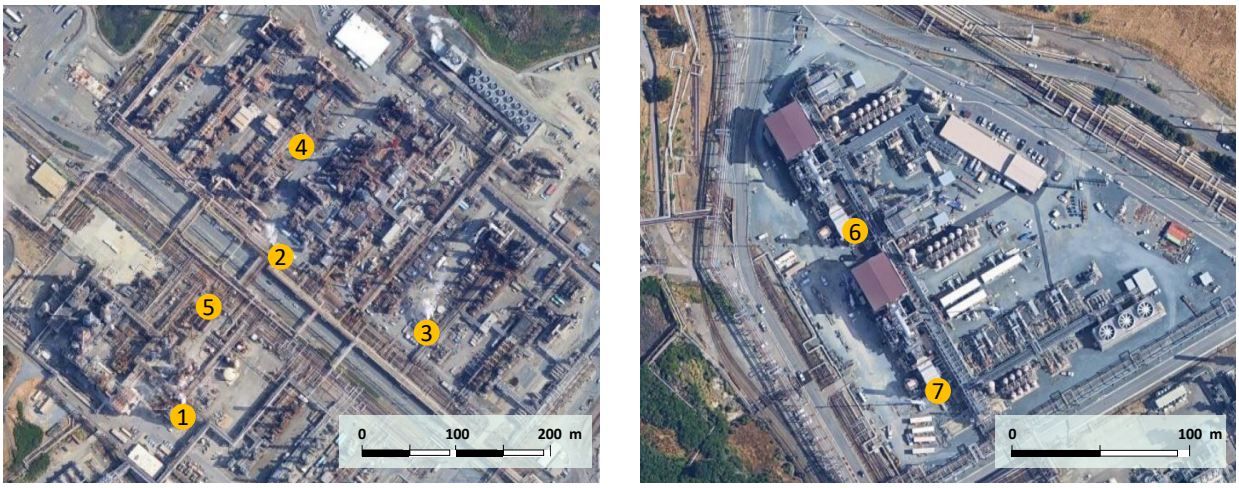

Figure C.2: Location of plume stacks in regions 1 (left) and 2 (right) as designated in Figure C.1.

Table C.2: Calculated stack heights for the stacks numbered in Figure C.2 using shadow lengths and directions from satellite imagery taken on different days. Omitted values are from instances when the shadow was not well defined, typically due to surrounding obstructions.

Stack #	May 12, 2023	June 28, 2022	Feb 11, 2022	Mean
1	15.1 m	–	10.8 m	12.9 m
2	8.5 m	11.4 m	7.8 m	9.2 m
3	–	–	15.8 m	15.8 m
4	10.4 m	11.6 m	–	11.0 m
5	6.2 m	7.2 m	–	6.7 m
6	–	33.1 m	34.0 m	33.5 m
7	–	33.6 m	36.6 m	35.1 m

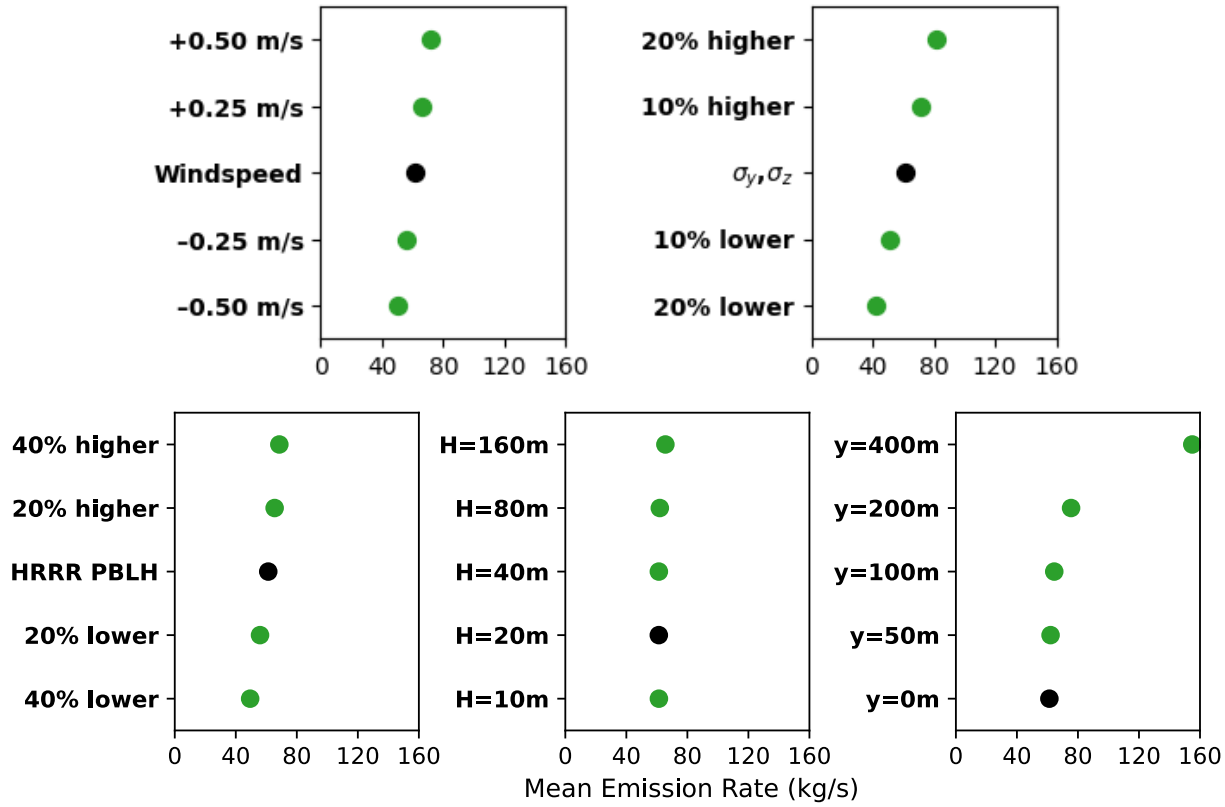

Figure C.3: Distribution of the emission rate estimated from the Gaussian plume model and multi-point source correction under alternative parameter scenarios (in green), with the base case (in black) as comparison. **Top Row:** On the left, windspeed is increased or decreased by different amounts compared to HRRRv4 model outputs, with the unaltered output used in this analysis. On the right, and are scaled up and down from the default parameterization used in this analysis. **Bottom Row:** On the left, the PBL height is scaled from HRRRv4 model outputs, with the unscaled output used in this analysis. In the middle, the emission height H is varied from 10 to 160 m, with 20 m being the value used in the analysis. On the right, y is varied from 0 to 500 m with y=0 being the default value used in the analysis.

Table C.3: CO_2 Plumes at the Chevron Richmond Refinery Identified and Quantified by Carbon Mapper.[146] Regions are defined in Figure C.1 Multiple plumes measured in the same region at the same time were combined.

Location	Date and Time	Emission Rate (kg CO_2/hr)
2	May 14, 2022 19:45 UTC	63,300 ± 17,000
2	May 14, 2022 19:40 UTC	85,400 ± 21,500
2	Oct 5, 2018 19:01 UTC	56,100 ± 24,100
2	Oct 5, 2018 19:49 UTC	199,700 ± 73,800
3	May 14, 2022 19:45 UTC	93,700 ± 16,600
3	May 14, 2022 19:40 UTC	117,900 ± 28,300
3	Sep 18, 2020 22:39 UTC	123,300 ± 15,400

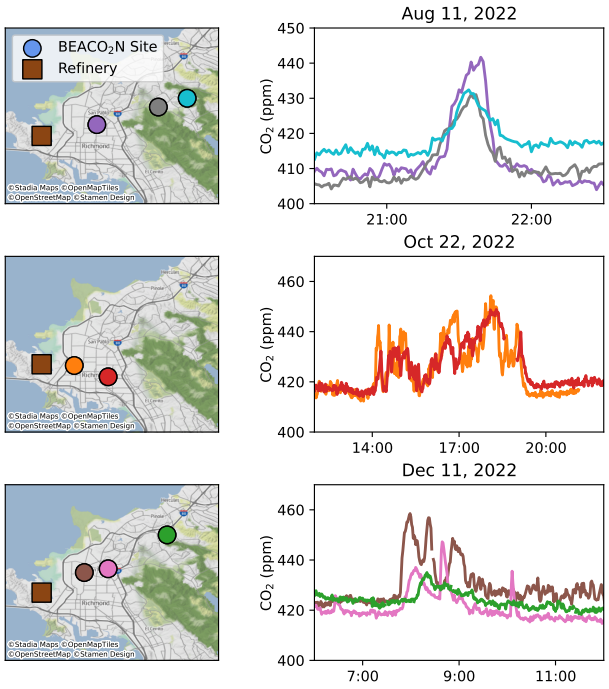

Figure C.4: Examples of coincident plume measurements for different sets of $BEACO_2N$ sites that linearly extend from the refinery site. Background map credits: © Stadia Maps (stadiamaps.com), © Stamen Design (stamen.com), © OpenMapTiles (openmaptiles.org), © OpenStreetMap (openstreetmap.org/copyright).

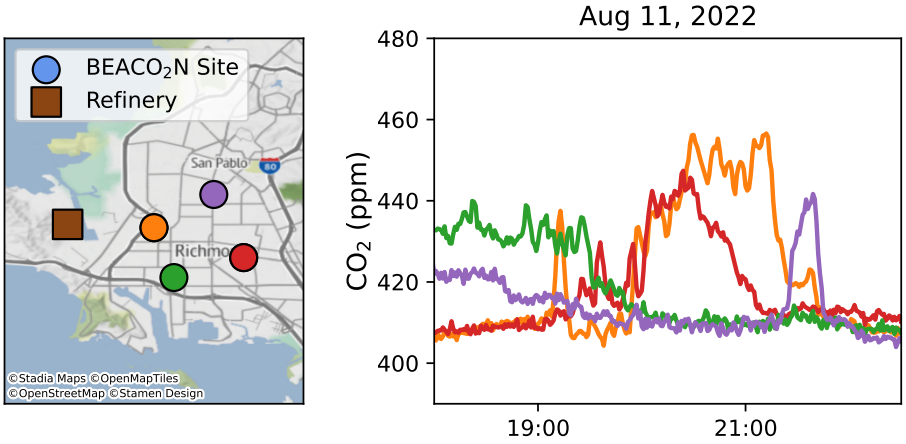

Figure C.5: Example of coincident plume measurements for different sets of $BEACO_2N$ sites that are consistent with a plume extending from the refinery rotating across the network. Background map credits: © Stadia Maps (stadiamaps.com), © Stamen Design (stamen.com), © OpenMapTiles (openmaptiles.org), © OpenStreetMap (openstreetmap.org/copyright).